*materials*

MDPI

*Article*

# Adsorption and Oxidation of CO on Ceria Nanoparticles Exposing Single-Atom Pd and Ag: A DFT Modelling

**Vladimir A. Nasluzov [1], Elena A. Ivanova-Shor [1,*], Aleksey M. Shor [1], Svetlana S. Laletina [1] and Konstantin M. Neyman [2,3]**

[1] Institute of Chemistry and Chemical Technology SB RAS, Federal Research Center "Krasnoyarsk Science Center SB RAS", 660036 Krasnoyarsk, Russia; v.nasluzov@yandex.ru (V.A.N.); am.shor@yandex.ru (A.M.S.); shkulepo@rambler.ru (S.S.L.)

[2] Departament de Ciència de Materials i Química Física and Institut de Quimica Teòrica i Computacional, Universitat de Barcelona, 08028 Barcelona, Spain; konstantin.neyman@icrea.cat

[3] ICREA (Institució Catalana de Recerca i Estudis Avançats), 08010 Barcelona, Spain

* Correspondence: eshor1977@gmail.com

**Abstract:** Various $CO_x$ species formed upon the adsorption and oxidation of CO on palladium and silver single atoms supported on a model ceria nanoparticle (NP) have been studied using density functional calculations. For both metals M, the ceria-supported $MCO_x$ moieties are found to be stabilised in the order MCO < $MCO_2$ < $MCO_3$, similar to the trend for $CO_x$ species adsorbed on M-free ceria NP. Nevertheless, the characteristics of the palladium and silver intermediates are different. Very weak CO adsorption and the small exothermicity of the CO to $CO_2$ transformation are found for $O_4Pd$ site of the $Pd/Ce_{21}O_{42}$ model featuring a square-planar coordination of the $Pd^{2+}$ cation. The removal of one O atom and formation of the $O_3Pd$ site resulted in a notable strengthening of CO adsorption and increased the exothermicity of the CO to $CO_2$ reaction. For the analogous ceria models with atomic Ag instead of atomic Pd, these two energies became twice as small in magnitude and basically independent of the presence of an O vacancy near the Ag atom. $CO_2$-species are strongly bound in palladium carboxylate complexes, whereas the $CO_2$ molecule easily desorbs from oxide-supported $AgCO_2$ moieties. Opposite to metal-free ceria particle, the formation of neither $PdCO_3$ nor $AgCO_3$ carbonate intermediates before $CO_2$ desorption is predicted. Overall, CO oxidation is concluded to be more favourable at Ag centres atomically dispersed on ceria nanostructures than at the corresponding Pd centres. Calculated vibrational fingerprints of surface $CO_x$ moieties allow us to distinguish between CO adsorption on bare ceria NP (blue frequency shifts) and ceria-supported metal atoms (red frequency shifts). However, discrimination between the $CO_2$ and $CO_3^{2-}$ species anchored to M-containing and bare ceria particles based solely on vibrational spectroscopy seems problematic. This computational modelling study provides guidance for the knowledge-driven design of more efficient ceria-based single-atom catalysts for the environmentally important CO oxidation reaction.

**Keywords:** $CeO_2$-based nanomaterials; density functional calculations; single-atom catalysts; structure; reactivity



**Citation:** Nasluzov, V.A.; Ivanova-Shor, E.A.; Shor, A.M.; Laletina, S.S.; Neyman, K.M. Adsorption and Oxidation of CO on Ceria Nanoparticles Exposing Single-Atom Pd and Ag: A DFT Modelling. *Materials* **2021**, *14*, 6888. https://doi.org/10.3390/ma14226888

Academic Editors: Simona Bennici and Ilenia Rossetti

Received: 22 October 2021
Accepted: 9 November 2021
Published: 15 November 2021



## 1. Introduction

Ceria, as a component of catalysts containing transition metals (M) Pd or Ag, is used in numerous applications ranging from the abatement of soot, volatile organic compounds, and CO [1–10] to the production of syngas [11] and $CO_2$ activation [12,13]. As an active reducible support, ceria facilitates the dispersion of metals and $MO_x$ phases on the surface [7,14–17] and provides lattice O atoms to oxidise reactants [2,9,17–20]. For instance, the interactions within Pd–ceria interfaces allow the synergistic oxidation/reduction of both subsystems [21], promote the oxidation of CO by lattice O atoms, and the oxidation of the reduced ceria by O atoms of $CO_2$ [22]. Supported transition metals can also enhance

the redox performance and oxygen storage capacity of ceria [23]. Often, high catalytic efficiency is achieved using a nanostructured ceria support via enhanced metal–support interaction, which improves the dispersion of metal particles and suppresses their sintering at elevated temperatures [3,4,7–9,11,19,24–27].

The M-containing surface phases of the aforementioned systems are represented by $M_m$ [6,7,16,24,28,29] and $MO_x$ [6,25,26,30] nanoparticles (NPs), charged metal clusters [7,24,31], solid $M_xCe_{1-x}O_{2-\delta}$ solutions [25–27,32–35], and dispersed $M_1$ or $O_xM_1$ ad-species [3,6–9,16,36,37]. Analysis of the crystalline environment of the $Pd_1$ ad-species revealed that each $Pd^{2+}$ ion in $Pd/CeO_2$ catalysts prepared by the solution combustion method is coordinated, on average, by three O atoms [34]. This coordination mode of $Pd_1$ is a feature of adsorption complexes with CO such as $O_2Pd_1$-$CO/CeO_2(111)$ [8], $O_1Pd_1$-$CO/CeO_2(111)$ [8], and $O_1Pd_1$-$CO/CeO_2(100)$ [9], while a $Pd_1$-$CO/CeO_2(100)$ complex exhibits an O-Pd-O bridge [9]. In many cases, $Pd_1$ is in a square-planar environment. $Pd_1$ centres in $Ce_{1-x}Pd_xO_{2-\delta}$ crystals ($x \leq 0.15$) reside on $O_4$ units adjacent to Ce centres [32]. The doping of ceria with Pd results in a structure with the dopant ion displaced from the initial cationic position to the centre of the $O_4$ unit [23]. Furthermore, $Pd_1$ species are attached to the $O_4$ unit of the $Pd_xCe_{1-x}O_{2-x-\delta}$ lattice incorporating products of water dissociation [27]. Replacing every second upper-layer $Ce^{4+}$ cation and one adjacent to it $O^{2-}$ anion on the $CeO_2(110)$ surface with $Pd^{2+}$ leads to a complex reconstruction and a low-energy surface geometry, with the dopant ion residing close to the centre of the square-planar $O_4$ site [6]. Stable structures with square-planar $O_4Pd$ are also communicated on Pd-doped $CeO_2(111)$ [33] and edges of ceria NPs at intersecting {111} and {100} nanofacets [35]. Four-fold coordinated Pd adatoms are identified in the most stable $O_4Pd$ structures on the $CeO_2(110)$ surface [20] and {100} nanofacets [37]. The surface $O_4$ sites are also capable of suppressing the sintering of $Ag_1$ species, despite the fact that the Ag atom binds to the {100}-$O_4$ pocket more weakly than other Group VIII–XI metal atoms [37,38]. The aforementioned thermally stable structures are relevant to the development of the single-atom catalysts [36,37,39].

To understand how the role of the ceria support varies in specific catalytic processes, it is crucial to examine the interactions of the involved reactants with various active centres of $CeO_2$. For the ceria-supported metal catalysts of CO oxidation or $CO_2$ activation, of primary interest are the interactions of $O_2$, CO, and $CO_2$ molecules with the metal–support interfaces [2,8,9,18,20,33,40–43]. Thus, modelling based on density functional theory (DFT) has recently addressed a variety of sites with $M_1$-$O_2$, $M_1$-CO, and $M_1$-$CO_2$ entities on ceria [8,9,18,20,40]. The adsorption of CO on a single Pd atom embedded in the defect-free $CeO_2(111)$ surface and that containing O vacancies followed by NO reduction with CO was explored [18,40]. Surface complexes of CO and $CO_2$ taking part in the catalytic cycle of CO oxidation on $Pd_1/CeO_2(110)$, including $Pd_1$-CO, $Pd_1$-$CO_2$, $O_1Pd_1$-CO species on the stoichiometric $CeO_2(110)$ surface and $Pd_1$-$CO_2$, $Pd_1$-$O_2$, $O_2$-$Pd_1$-CO ones on the O-deficient $CeO_2(110)$ surface, were calculated [20]. The CO oxidation routes passing via $O_1Pd_1$-CO, $Pd_1$-CO, $Pd_1$-$CO_2$, $O_2Pd_1$-CO, and $O_1Pd_1$-$CO_2$ moieties on the defect-free $CeO_2(111)$ surface [8] as well as on regular and O-deficient $CeO_2(100)$ surfaces [9] were also quantified. The catalytic CO oxidation according to the Mars-van-Krevelen mechanism combines the elementary steps of oxygen donation from a surface active centre to adsorbed CO and the subsequent replenishment of the support by stream oxygen; the much slower conversions of the first step are found to be rate-determining [8,9,19,20]. In addition to the $M_1$-$CO_2$ structures, surface carbonate complexes can be formed on $M_1$–ceria interfaces before the desorption of $CO_2$. To this end, the formation of tridentate $Pd_1$-$CO_3$ carbonates upon $CO_2$ adsorption at the interface of $Pd_1$ and O-deficient $CeO_2(111)$ surface was simulated [13] and the CO vibration frequencies of various ceria-supported Pd-CO species were calculated [8,9]. Unlike the quite extensive computational studies of $Pd_1CO_x$–ceria systems outlined above, no simulations of analogous $Ag_1CO_x$–ceria systems have been communicated so far to the best of our knowledge.

Previous studies have developed structural models of low-energy $CeO_2$ NPs [44–47] and established that their {100} nanofacets notably stabilise single d-metal atoms [38,41,44,48–51]. In this work, we consider monoatomic Pd and Ag species located on a $Ce_{21}O_{42}$ NP [49] as models appropriately describing surface composites formed by single-atom Pd and Ag with nanostructured ceria. These two metals, which are neighbouring in the Periodic Table, interact very differently with ceria and behave as M-based species involved in CO oxidation. The quantification and in-depth understanding of such differences are still missing in the literature.

This study aims to (i) determine the structures of the lowest-energy complexes with CO, $CO_2$, and $CO_3^{2-}$ moieties resulting from the interaction of CO with Pd and Ag single atoms anchored to the $O_4$-pocket sites of the stoichiometric and O-deficient ceria NPs, (ii) analyse the structure and properties of these nanostructured adsorption systems versus earlier investigated analogues formed on extended ceria surface containing $M_1$ centres, (iii) evaluate and rationalise the reactivity differences of $Pd_1$/NP{100} and $Ag_1$/NP{100} sites as active centres for CO oxidation (including the effect of M-atom on the formation of $CO_3^{2-}$ prior to $CO_2$ desorption), and (iv) examine the vibrational fingerprints of the $CO_x$ units accompanying the formation of various surface species. Obtained results related to all these aspects are summarised in the Conclusions section.

## 2. Models and Details of Calculations

Surface sites of the $CeO_2$ substrate were represented by a putative global-minimum structure of stoichiometric NP $Ce_{21}O_{42}$ [46,47] exposing four O atoms on its top {100} nanofacet (a so-called $O_4$-pocket [49]); see Figure 1a. $M_1/Ce_{21}O_{42}$ models were created via anchoring a single $M_1$ atom (M = Pd or Ag) to the $O_4$-site of the NP; see Figure 1b,c. The removal of one O atom from the $O_4$-pocket results in an O-deficient $M_1/Ce_{21}O_{41}$ model with one O vacancy in ceria (not shown in Figures; see Supplementary Material for xyz-structures). CO adsorption does not change the number of O vacancies, whereas the oxidation of CO to $CO_2$ and further transformation to $CO_3^{2-}$ require the expulsion of one or two O atoms from ceria, generating O vacancies. In the following, the number and origin of O vacancies in the NP $Ce_{21}O_{42}$ are labelled as NP[$n/l$], where $n$ is a number of O vacancies present prior to CO adsorption ($n$ = 0, 1) and $l$ is a number of O vacancies created by the transfer of O atoms from ceria to the adsorbed CO to form $CO_2$ or $CO_3^{2-}$ moieties ($l$ = 0, 1, 2). For instance, the stoichiometric and O-deficient NP models $M_1/Ce_{21}O_{42}$ and $M_1/Ce_{21}O_{41}$ are referred to as M/NP[0/0] and M/NP[1/0], respectively.

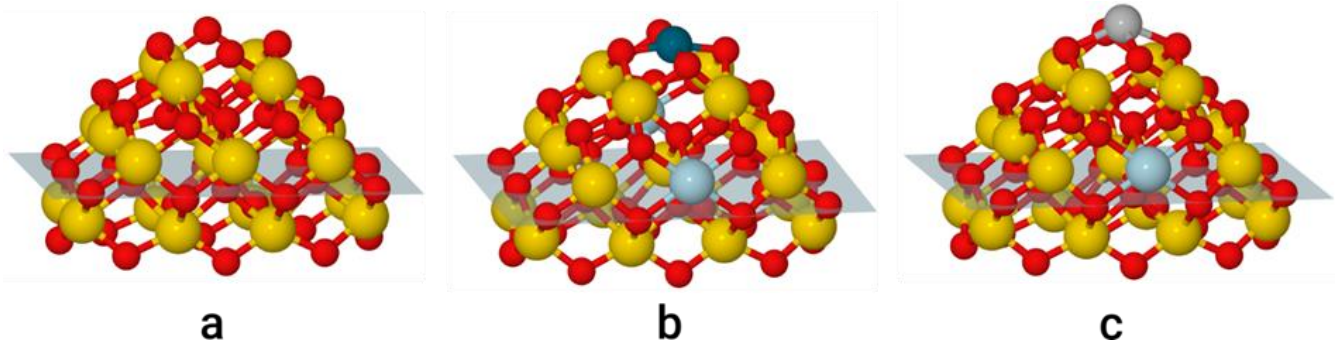


**Figure 1.** Models of $Ce_{21}O_{42}$ NP: (**a**) without metal atom; (**b**) with Pd atom anchored at {100} facet; (**c**) with Ag atom anchored at {100} facet. The $Ce^{4+}$, $Ce^{3+}$, Pd, Ag, and O atoms are shown in yellow, light blue, dark cyan, grey, and red, respectively. The atoms under the transparent plane are omitted for clarity in the Figures 2–4.

The Vienna ab initio simulation package (VASP) [52,53] was employed to determine equilibrium structures of various isomers of the $MCO_x$/NP[$n/x-1$] complexes formed by the interaction of a CO molecule with Pd/NP[$n$/0] and Ag/NP[$n$/0] sites and transition state structures connecting selected equilibrium structures. The plane-wave basis with a 415 eV cutoff for the kinetic energy was used along with the projector-augmented wave

description of the interactions of valence electrons ($2s^2 2p^4$ for O, $4s^1 4d^9$ for Pd, $5s^1 4d^{10}$ for Ag and $5s^2 5p^6 6s^2 5d^1 4f^1$ for Ce) with the atomic cores [54,55]. The NP models were separated by a vacuum space of ~1 nm in the three Cartesian directions (typical cell dimensions $2 \times 2 \times 2$ nm$^3$) sufficient to eliminate the interaction between periodically repeated NP images [56,57]. All calculations were performed at the Γ-point of the reciprocal space. A generalised-gradient corrected (GGA) exchange-correlated functional PW91 [58] was utilised with the Hubbard-type on-site corrections U [59,60] for Ce4f states providing an improved description of $Ce^{3+}$ ion formation in redox transitions [61,62]. The value of U = 4 eV (PW91 + U = 4 setup) were used in line with previous studies [45,48,61,63,64], though the usage of even such small U values may overestimate the formation energy of carbonates [62,65]. The minimum energy reaction paths MCO/NP[$n$/0] → $MCO_2$/NP[$n$/1] → $MCO_3$/NP[$n$/2] were represented with the points of the string method, and the transition states were approximated with polynomial splines [66,67].

Stabilities of the studied systems were quantified based on their formation energies $E^f$:

$$E^f = E(MCO_x/NP[0/x-1]) - E(CO) - E(M) - E(NP[0/0]) \quad (1)$$

for the $MCO_x$/NP models obtained from defect-free MCO/$Ce_{21}O_{42}$ structure and

$$E^f = E(MCO_x/NP[1/x-1]) - E(CO) - E(M) - E(NP[0/0]) + 0.5 \times E(O_2) \quad (2)$$

for the $MCO_x$/NP models obtained from O-deficient MCO/$Ce_{21}O_{41}$ structure, where $E(O_2)$ is total energy of a free $O_2$ molecule. The binding energies $E_b$ of CO and $CO_2$ molecules in the models under scrutiny were calculated as follows:

$$E_b(CO) = E(MCO_x/NP[n/x-1]) - E(CO) - E(M/NP[n/0]),\ x = 1\text{–}3;\ n = 0,\ 1 \quad (3)$$

$$E_b(CO_2) = E(MCO_x/NP[n/x-1]) - E(CO_2) - E(M/NP[n/1]),\ x = 2,\ 3;\ n = 0,\ 1 \quad (4)$$

The energies (3) and (4) of the same $MCO_2$/NP complex were used to estimate the energy of the overall oxidation process CO(gas) + M/NP[$n$/0] → $CO_2$(gas) + M/NP[$n$/1]:

$$E_{ox} = E_b(CO)(MCO_2/NP[n/1]) - E_b(CO_2)(MCO_2/NP[n/1]) \quad (5)$$

or

$$E_{ox} = E_b(CO)(MCO/NP[n/0]) + E^*_{CO2} - E_b(CO_2)(MCO_2/NP[n/1]),\ n = 0,\ 1 \quad (6)$$

where $E^*_{CO2}$ is the energy of CO to $CO_2$ oxidation at a metal site; i.e., the heat of MCO/NP[$n$/0] → $MCO_2$/NP[$n$/1] transformation:

$$E^*_{CO2} = E(MCO_2/NP[n/1]) - E(MCO/NP[n/0]) \quad (7)$$

where, the asterisk indicates that CO and $CO_2$ molecules are adsorbed.

Harmonic vibrational frequencies of $CO_x$ groups were calculated by diagonalising the mass-weighted Hessian matrix constructed of differences of the first derivatives of total energy, obtained by displacements by ±0.015 Å in all Cartesian directions of the M, C, and $O_x$ atoms as well as neighbouring ceria atoms within 3.6 Å around them.

## 3. Results and Discussion

Lowest-energy geometries and formation energies $E^f$ of metal-free $CO_x$/NP[$n/x-1$] and metal-containing $MCO_x$/NP[$n/x-1$] complexes are shown in Figures 2–4 (for xyz-structures see Supplementary Material). Table 1 displays the parameters used to specify attachment modes (coordination) of the $CO_x$ groups. Along with the notations $MCO_x$/NP[$n/x-1$], shorter ones **MxL** and **MxLV** were used for complexes with $n$ = 0 and $n$ = 1, respectively, where **L** is a sequential identifier of the relative energy of a given isomer among isomers with the same **M**, **x**, and **n** (**a**—the most stable, **b**—the second most

stable, **c**—the third most stable). Ce ions with magnetic moments close to 1, at a variance to 0 for most of the cations, were qualified as $Ce^{3+}$ ions resulting from the reduction of $Ce^{4+}$ by electrons of $MCO_x$ moieties or O vacancies.

**Table 1.** Calculated parameters of the surface complexes shown in Figures 2–4, created by the interaction of CO with the pristine ceria $Ce_{21}O_{42-n}$ and metal–ceria $M/Ce_{21}O_{42-n}$ sites (M = Pd, Ag; $n$ = 0, 1): interatomic distances—r, number of the $Ce^{3+}$ ions—N, difference between the numbers of spin-up and spin-down electrons—m, binding energies of CO—$E_b(CO)$ (Equation (3)) and $CO_2$–$E_b(CO_2)$ (Equation (4)). Negative energy values correspond to exothermic processes.

| System [a] | r(M-C) pm | r(M-O) pm | r(Ce-O) [b] pm | r(C-O) [c] pm | N | m | $E_b(CO)$ eV | $E_b(CO_2)$ eV |
|---|---|---|---|---|---|---|---|---|
| Complexes with CO | | | | | | | | |
| **Pd1a** | 296 [d] | - | - | 114 | 2 | 2 | −0.26 | - |
| **Pd1b** | 241 | - | - | 115 | 2 | 2 | −0.13 | - |
| **Pd1c** | 188 | - | - | 116 | 1 | 0 | 0.13 | - |
| **Pd1aV** | 187 | - | - | 116 | 4 | 4 | −1.74 | - |
| **Ag1a** | 201 | - | - | 115 | 1 | 1 | −0.80 | - |
| **Ag1aV** | 198 | - | - | 115 | 3 | 3 | −0.78 | - |
| **1a** | 293 [d] | - | - | 114 | 0 | 0 | −0.26 | - |
| **1aV** | 297 [d] | - | - | 114 | 2 | 2 | −0.23 | - |
| Complexes with $CO_2$ | | | | | | | | |
| **Pd2a** | 206 | - | 247 | 2 × 127 | 2 | 0 | −1.43 | −1.20 |
| **Pd2b** | - | - | 314 | 2 × 118 | 2 | 0 | −0.41 | −0.18 |
| **Pd2aV** | 193 | 237 | 268 | 129; 124 | 4 | 4 | −2.33 | −0.72 |
| **Pd2bV** | 330 | - | 321 | 2 × 118 | 4 | 4 | −1.77 | −0.16 |
| **Ag2a** | 356 | - | 316 | 2 × 118 | 3 | 3 | −1.37 | −0.16 |
| **Ag2b** | 234 | - | 268 | 122; 121 | 3 | 1 | −1.22 | −0.01 |
| **Ag2aV** | 207 | - | 249 | 2 × 132 | 3 | 1 | −1.13 | −0.10 |
| **Ag2bV** | 342 | - | 348 | 2 × 118 | 5 | 1 | −1.10 | −0.07 |
| **2a** | - | - | 300 | 2 × 118 | 2 | 0 | −1.69 | −0.25 |
| **2aV** | - | - | 310 | 2 × 118 | 4 | 2 | −1.16 | −0.15 |
| **2bV** | - | - | 254 | 2 × 125 | 3 | 2 | −0.42 | 0.59 |
| Complexes with $CO_3^{2-}$ | | | | | | | | |
| **Pd3a** | 249 | 207 | 260 | 2 × 133; 125 | 4 | 2 | −1.68 | −1.44 |
| **Pd3b** | 265 | 209 | 248 | 129; 135; 129 | 3 | 2 | −0.99 | −0.75 |
| **Pd3c** | - | 212 | 245 | 133; 143; 121 | 2 | 0 | −0.74 | −0.50 |
| **Pd3aV** | 275 | 211 | 258 | 132; 132; 128 | 4 | 2 | −2.67 | −1.06 |
| **Pd3bV** | 288 | 211 | 247 | 131; 143; 122 | 4 | 0 | −2.28 | −0.67 |
| **Ag3a** | 277 | 221 | 245 | 130; 135; 127 | 3 | 1 | −2.72 | −1.49 |
| **Ag3b** | 289 | 233 | 247 | 132; 141; 122 | 3 | 1 | −2.09 | −0.86 |
| **Ag3aV** | 273 | 216 | 265 | 130; 132; 130 | 5 | 1 | −2.36 | −1.40 |
| **Ag3bV** | 291 | 211 | 255 | 129; 146; 122 | 5 | 1 | −2.09 | −1.13 |
| **3a** | - | - | 237 | 133; 138; 122 | 2 | 0 | −2.59 | −1.15 |
| **3b** | - | - | 250 | 129; 132; 129 | 2 | 2 | −2.28 | −0.84 |
| **3aV** | - | - | 262 | 130; 131; 130 | 4 | 2 | −3.23 | −2.22 |
| **3bV** | - | - | 229 | 133; 137; 122 | 4 | 2 | −2.53 | −1.52 |

[a] For notations, see Figures 2–4; [b] Average distances of the O of $CO_x$ moiety and nearest neighbour Ce atom; [c] Bond lengths within $CO_x$ moiety; [d] Ce-C contact.

To specify the coordination modes of $CO_2$ in $MCO_2/NP[n/1]$ and of $CO_3^{2-}$ in $MCO_3/NP[n/2]$ complexes, additional three-digit indices were used [68] resulting in the notation that being invoked only when discussing the coordination modes of $CO_x$ species. For carbonate complexes, a notation abc (integer a, b and c range from 0 to 3) determines numbers of substrate atoms, to which each O atom in $CO_3^{2-}$ is coordinated. The middle digit b corresponds to the O atom with the highest coordination. A dot in indices a.bc or ab.c specifies that two O atoms of $CO_3^{2-}$ (corresponding to a and b or b and c, respectively) form a bidentate bond with one atom of the substrate. Dotless abc identifiers designate $CO_3^{2-}$ groups with each O atom coordinated to a different substrate atom. When the three-digits notation is used to specify coordination of $CO_2$ in $MCO_2/NP[n/1]$

complexes, the first digit a gives the number of substrate atoms coordinated to C atom. For instance, in Figure 3, each of the atoms of $CO_2$ in structure 111-**Pd2a** contacts different ions of the $Pd/Ce_{21}O_{41}$ subsystem, and in complex 1.21-**Pd2aV**, one of the O atoms of $CO_2$ attaches to Pd and Ce atoms of $Pd/Ce_{21}O_{40}$, and C atom also to Pd.

### *3.1. Structure, Charge State, and Relative Energies of Surface Complexes with $CO_x$*

#### 3.1.1. Adsorption Sites

The particle $Ce_{21}O_{42}$ exposes a {100} nanofacet (Figure 1a), which can bind metal atoms much stronger than its {111} nanofacets do [38]. We anchored single Pd and Ag atoms to the {100} nanofacet composed of four nearly coplanar two-coordinated oxygen centres forming an $O_4$-pocket with diagonals of 459 and 443 pm. This arrangement is appropriate for accommodating transition metal cations with typical M-O bond lengths of 185–210 pm [37]. The distances between the $O_4$-pocket atoms and the neighboring Ce atoms, 214–215 pm, are shortened versus the Ce-O distances of three-coordinated surface O atoms and four-coordinated inner O atoms, 230–250 pm.

The Ag atom binds by 2.27 eV to the $O_4$-site (Figure 1b), making the two diagonals of the latter almost equal. The two types of Ag-O bond lengths, 236 and 242 pm, agree with Ag-O distances of 239 and 241 pm calculated at the same theory level on a larger $Ce_{40}O_{80}$ NP [37]. Furthermore, the present location of the Ag atom 96 pm above the $O_4$-plane is close to the elevation by 90 pm on $Ce_{40}O_{80}$ [37]. A slightly larger above-plane elevation, by 102 pm, was calculated for a two-fold coordinated Ag single atom adsorbed on the $Fe_3O_4(001)$ surface with energy 2.75 eV [69]. Ag atom adsorption moves $O_4$ centres upwards, elongating the involved Ce-O distances to 218–223 pm. One Ce ion reduced to +3 state, pointing to the $Ag^+$ oxidation state.

The Pd adatom is located nearly in the $O_4$ plane (Figure 1c), with an out-of-plane displacement of 18 pm, adopting a favourable planar coordination. All four Pd-O bonds are equal to 205 pm—exactly the same as for the $Pd/Ce_{40}O_{80}$ model [37]. The formation of $PdO_4$ species moves O atoms closer to Pd, contracting diagonals of the $O_4$ square to 408 pm and elongating the corresponding Ce-O distances to 230 pm—the value typical for three-coordinated O centres. The high adsorption energy of the Pd atom, 4.24 eV, further increases upon interactions with the $O_4$-site of larger ceria NPs [37]. Two $Ce^{3+}$ ions appeared upon Pd adsorption, indicating the oxidation state $Pd^{2+}$.

An O-deficient site is created by the removal of the weakest bonded O atom (with $E(O_V)$ = 1.87 eV, Table 2) from the $O_4$-pocket of the $Ce_{21}O_{42}$ particle (Figure 1). Two $Ce^{3+}$ centres resulting from the O removal in the second Ce layer cause the elongation of the $Ce^{3+}$-O bonds by ~0.1 Å. O vacancy formation in the $Ag/Ce_{21}O_{42}$ model requires 2.08 eV (Table 2), nearly the same amount as for the metal-free $O_4$-site. Thus, an extra energy cost due to breaking the Ag-O bond (in addition to two Ce-O bonds of $Ce_{21}O_{42}$) is estimated at ~0.2 eV. Two Ag-O bonds are contracted to 2.15 Å upon O removal, whereas the third bond is elongated from 2.36 to 2.49 Å. A similar bonding situation has been found in our previous work, where an Ag single atom was anchored to the bottom {100} nanofacet of $Ce_{21}O_{42}$ NP [38]. Alternatively, the creation of an O-deficient $Pd/Ce_{21}O_{41}$ site requires substantial energy costs of 3.08 eV (Table 2).

**Table 2.** Reaction and activation energies ($E^{\neq}$) on the pristine ceria $Ce_{21}O_{42-n}$ and metal–ceria $M/Ce_{21}O_{42-n}$ models (M = Pd, Ag; $n$ = 0, 1) depicted in Figures 2–4. Oxygen vacancy formation energies $E(O_V)$ are also shown. Negative energy values correspond to exothermic processes. All energies are in eV.

| Model [a] | | $CO \rightarrow CO_2$ | | | $CO_2 \rightarrow CO_3$ | |
|---|---|---|---|---|---|---|
| | $E(O_V)$ | $E_{ox}$ [b] | $E^*_{CO2}$ [c] | $E^{\neq}$ | $E^*_{CO3}$ [d] | $E^{\neq}$ |
| $Ce_{21}O_{42}$ | 1.87 | −1.44 | −1.43 | 1.02 | −0.90 | 0.27 |
| $Ce_{21}O_{41}$ | 2.31 | −1.01 | −0.92 | 0.82 | −2.07 | 0.82 |
| $Ag/Ce_{21}O_{42}$ | 2.08 | −1.21 | −0.52 | 0.88 | −1.50 | 0.78 |
| $Ag/Ce_{21}O_{41}$ | 2.28 | −1.03 | −0.35 | 0.53 | −1.23 | 1.73 |
| $Pd/Ce_{21}O_{42}$ | 3.08 | −0.23 | −1.30 | 0.51 | −0.25 | 1.83 |
| $Pd/Ce_{21}O_{41}$ | 1.70 | −1.61 | −0.59 | 1.06 | −0.34 | 1.80 |

[a] System on which initial CO adsorption takes place; [b] reaction energy of the CO oxidation CO(gas) + NP[$n$/0] → $CO_2$(gas) + NP[$n$/1] or CO(gas) + M/NP[$n$/0] → $CO_2$(gas) + M/NP[$n$/1]; [c] reaction energy of the $CO_2$ formation CO/NP[$n$/0] → $CO_2$/NP[$n$/1] or MCO/NP[$n$/0] → $MCO_2$/NP[$n$/1]; [d] reaction energy of $CO_2$/NP[$n$/1] → $CO_3$/NP[$n$/2] or $MCO_2$/NP[$n$/1] → $MCO_3$/NP[$n$/2] conversion.

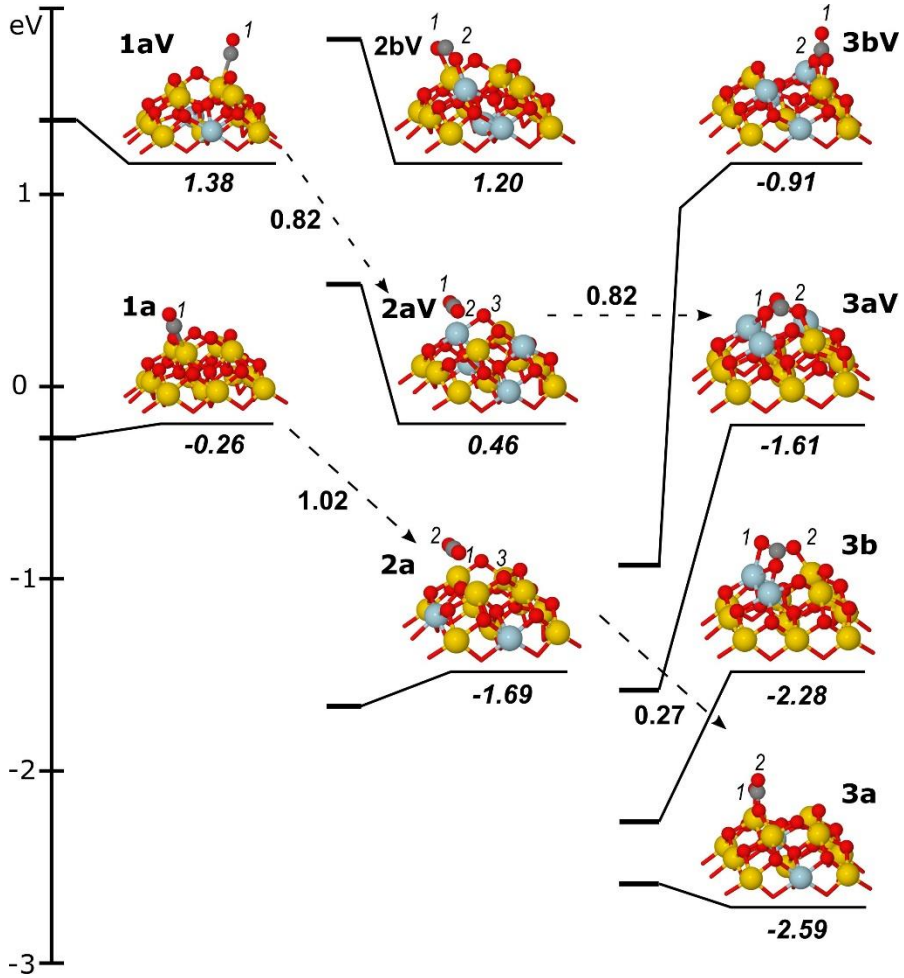


**Figure 2.** Structures and formation energies $E^f$ (in eV) of the complexes created by the interaction of CO with the $Ce_{21}O_{42-n}$ sites ($n$ = 0, 1): $CO/Ce_{21}O_{42}$ (**1a**), $CO/Ce_{21}O_{41}$ (**1aV**), $CO_2/Ce_{21}O_{41}$ (**2a**), $CO_2/Ce_{21}O_{40}$ (**2aV, 2bV**), $CO_3/Ce_{21}O_{40}$ (**3a, 3b**) and $CO_3/Ce_{21}O_{39}$ (**3aV, 3bV**). Activation energies ($E^{\neq}$) of selected transition states are shown near the dashed arrows connecting corresponding initial reagent and product. The C atoms are shown in dark grey. O atoms numbered with "1", "2", and "3" enter CO, $CO_2$, and $CO_3$ moieties, respectively. For further explanations, refer to the main text and the Figure 1 caption.

Evidently, an extra energy of ~1.2 eV is needed to cleave one Pd-O bond. Note that the Pd atom remains after O removal in a virtual square-planar environment with one coordination site empty and the lengths of the remaining three Pd-O bonds unchanged, 206–209 pm, vs. the $PdO_4$ site of $Pd/Ce_{21}O_{42}$. No reduction of $Ag^+$ and $Pd^{2+}$ ions occurs upon O vacancy creation, since the leaving O atom donates two electrons to two $Ce^{4+}$ ions, increasing the number of $Ce^{3+}$ centres by two (to three for Ag/NP and to four for Pd/NP).

#### 3.1.2. Carbonyl Species

Let us first consider the adsorption of a CO molecule on a Ce ion of bare ceria particles (Figure 2). For both the pristine and O-deficient structures, CO adsorption energy is very small, at −0.26 and −0.23 eV, respectively (Table 1). No geometry changes are calculated upon bringing together the CO molecule and ceria species. In particular, the C-O bond is retained at 114 pm as in the free CO molecule. The C end of the CO adsorbate is 293 (**1a**) and 297 pm (**1aV**) away from the nearest $Ce^{4+}$ ion of NP (Table 1). CO forms angles at 176° and 172° with the Ce site. Thus, CO is rather physisorbed than chemisorbed on the Ce site of the pristine and reduced forms of the metal-free NP. The same geometry and adsorption energy of −0.26 eV (Table 1) was calculated for the Pd-containing **Pd1a** structure with the CO molecule bound to a $Ce^{4+}$ ion (Figure 3), indicating that the filling of the $O_4$-pocket by the Pd atom mainly affects the local structure of the $PdO_4$ site.

An even smaller CO adsorption energy, −0.13 eV, was calculated for the coordinatively saturated Pd centre of the $PdO_4$ site of the unreduced model (**Pd1b**, Figure 3). Here, CO binds the Pd atom at an angle of 131° and rather long Pd–C contact of 241 pm.

CO adsorption causes minor distortions in the $Pd/Ce_{21}O_{42}$ structure: Pd-O bonds extend from 205 to 207 pm, and Pd moves by 27 pm above the $O_4$ plane. The C-O bond elongates by just 1 pm vs. gas-phase CO. No CO adsorption was reported on Pd atoms in the $PdO_4$ environment saturated by two O centres of the $CeO_2${100} surface and two O adatoms [9]. Furthermore, $E_b(CO) < -0.2$ eV was calculated for coordinatively saturated Pd atoms in PdO(100). Thus, a very low $E_b(CO)$ for **Pd1b** is related to the saturation of the coordination sphere of the Pd atom in the $O_4$-pocket of the {100} nanofacet by O atoms; the formation of an additional Pd-C bond competes with quite strong Pd-O bonds. The exceptional stability of $Pd^{2+}$ ions in square-planar oxygen environment in $CeO_2$ materials is also claimed in other experiments [6,27,32]. Note that CO adsorption on all Pd-containing models does not change the oxidation state $Pd^{2+}$, except for **Pd1c** with an endothermic mode by 0.13 eV CO adsorption (Table 1), where a $Ce^{3+} \rightarrow Ce^{4+}$ transition indicated a reduction to $Pd^+$.

In an O-deficient structure, **Pd1aV** (Figure 3), the adsorbed CO occupies one of four places around Pd. This results in Pd-C bond shortening to 187 pm (Table 1), as in $Pd_1$-$CO/CeO_2$(110) complexes bonded with two (Pd-C = 184 pm) and three O surface atoms (Pd-C = 188 pm) [20]. The Pd-C-O angle in **Pd1aV** is close to 180°. The elongation of the C-O distance from 114 to 116 pm indicates noticeable d → 2π* back-donation. In **Pd1aV**, CO binds at a vacant coordination site around Pd, no bonds are broken, and adsorption induced geometry changes are minor. As a result, $PdCO/Ce_{21}O_{41}$ is stabilised by 1.7 eV with respect to separated $Pd/Ce_{21}O_{41}$ and CO fragments (Table 1). Interestingly, similarly strong CO binding as that for **Pd1aV**, 1.77 eV, and a Pd-C distance of 186 pm were calculated for the two-fold coordinated single Pd atom in $Pd_1/Fe_3O_4$(001) [69]. The CO bond to the isolated Pd atom is also similarly strong, at 1.8 eV [70]. The values of 1.6 eV [8] and 1.9 eV [9] were calculated for $Pd_1$-$CO/CeO_2$(111) and $O_1Pd_1$-$CO/CeO_2$(100) complexes, respectively, with $Pd_1$ coordinated to three O atoms including that of isolated $O_1Pd_1$ species. A CO adsorption energy of −1.5 eV was calculated for the $Pd_1$-$CO/CeO_2$(110) complex with the $Pd^+$ ion between two three-fold O atoms [20]. In the series of complexes $Pd_1$-$CO/CeO_2$(111), $O_1Pd_1$-$CO/CeO_2$(111), and $O_2Pd_1$-$CO/CeO_2$(111), $E_b(CO)$ decreases (by module) with the growth of the $Pd_1$ coordination number from 1.6 to 0.9 and to 0.6 eV [8].

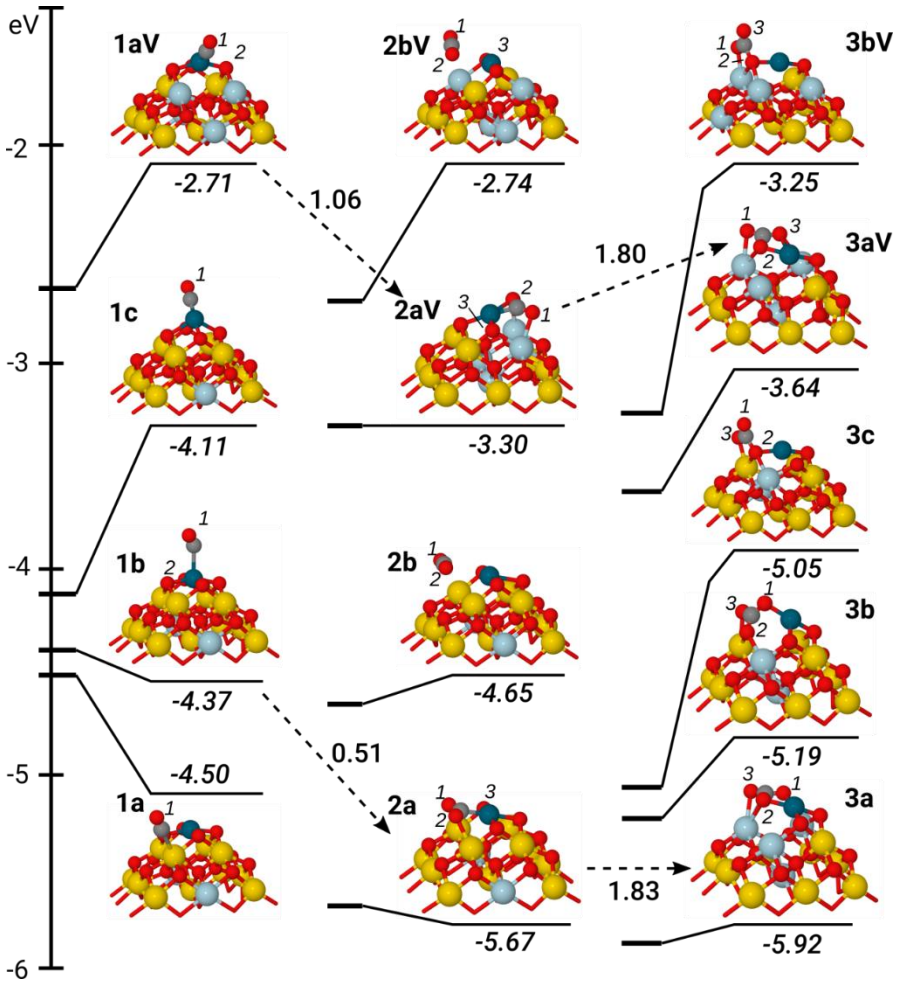


**Figure 3.** Structures and formation energies $E^f$ (in eV) of the complexes created by the interaction of CO with the $PdCe_{21}O_{42-n}$ sites ($n$ = 0, 1): $PdCO/Ce_{21}O_{42}$ (**Pd1a, Pd1b, Pd1c**), $PdCO/Ce_{21}O_{41}$ (**Pd1aV**), $PdCO_2/Ce_{21}O_{41}$ (**Pd2a, Pd2b**), $PdCO_2/Ce_{21}O_{40}$ (**Pd2aV, Pd2bV**), $PdCO_3/Ce_{21}O_{40}$ (**Pd3a, Pd3b, Pd3c**) and $PdCO_3/Ce_{21}O_{39}$ (**Pd3aV, Pd3bV**). Activation energies ($E^{\neq}$) of selected transition states are shown near the dashed arrows connecting corresponding initial reagent and product. For further explanations, refer to the main text and the captions to Figures 1 and 2.

The binding of CO to O-defect-free **Ag1a** and O-deficient **Ag1aV** complexes is moderately strong, at about 0.8 eV (Table 1), and essentially independent of the coordination—$AgO_4$ or $AgO_3$—of the Ag atom. This adsorption energy value fits the calculated values of −0.85 eV for CO adsorption at the two-fold coordinated Ag single atom in the $Ag_1/Fe_3O_4(001)$ site and −0.94 eV for the two-fold coordinated Ag atom at the $AgO_2(111)$ surface well [69]. Structures of the AgCO fragments in **Ag1a** and **Ag1aV** are very similar (Figure 4). The Ag-C distance of ~200 pm (Table 1) coincides with the value computed for the $Ag_1CO$ moiety at $Fe_3O_4(001)$. The C-O bond, 115 pm, is 1 pm longer than that in the free CO molecule. The Ag-C-O angle of ~170° points to slight deviation from the typically favoured linear bonding geometry. In both structures, CO adsorption triggers a further displacement of Ag atom out-of-plane of neighbouring O atoms, reaching values of 132 and 152 pm for **Ag1a** and **Ag1aV**, respectively (vs. 96 and 60 pm for CO-free structures). Ag-O bond lengths vary substantially, ranging from 237 to 258 pm for the $AgO_4$ unit and from 224 to 264 pm for the $AgO_3$ unit. The notable distortions at the $Ag/CeO_2$ interface are not reflected in CO adsorption energies. This finding is in line with the quite weak Ag-O bonding estimated at 0.2 eV (see Section 3.1.1).

In summary, the modification of the ceria NP with single Pd and Ag atoms strongly affects its affinity to CO. Effects of Pd and Ag atoms are different. Due to strong Pd-O

bonds, the saturated $PdO_4$ site is almost inactive towards CO adsorption, whereas the $PdO_3$ unit with a vacant coordination place readily traps CO with a substantial energy gain. In contrast, $AgO_4$ and $AgO_3$ centres with weak Ag-O bonds and a more flexible geometry are more prone to adsorb CO molecules with equally moderate energies.

#### 3.1.3. Carbon Dioxide Species

For the metal-free ceria, only weakly adsorbed $CO_2$ species were calculated: binding energies are −0.25 and −0.15 eV for **2a** and **2aV** models, respectively (Table 1). These energies are comparable with the values calculated for linearly-adsorbed $CO_2$ at extended $CeO_2$(100), (110), and (111) surfaces [71–76]. In both complexes, the linear geometry of $CO_2$ as in the gas-phase molecule is preserved: C-O bond lengths are 118 pm and the O-C-O angle is 178°. The C atoms of $CO_2$ molecules are located above the O vacancy parallel to the surface of NP (Figure 2); in case of **2a**, the O atom from the low-lying layer moves up and forms an O-C contact of 288 pm (vs. 390 pm in **2aV**).

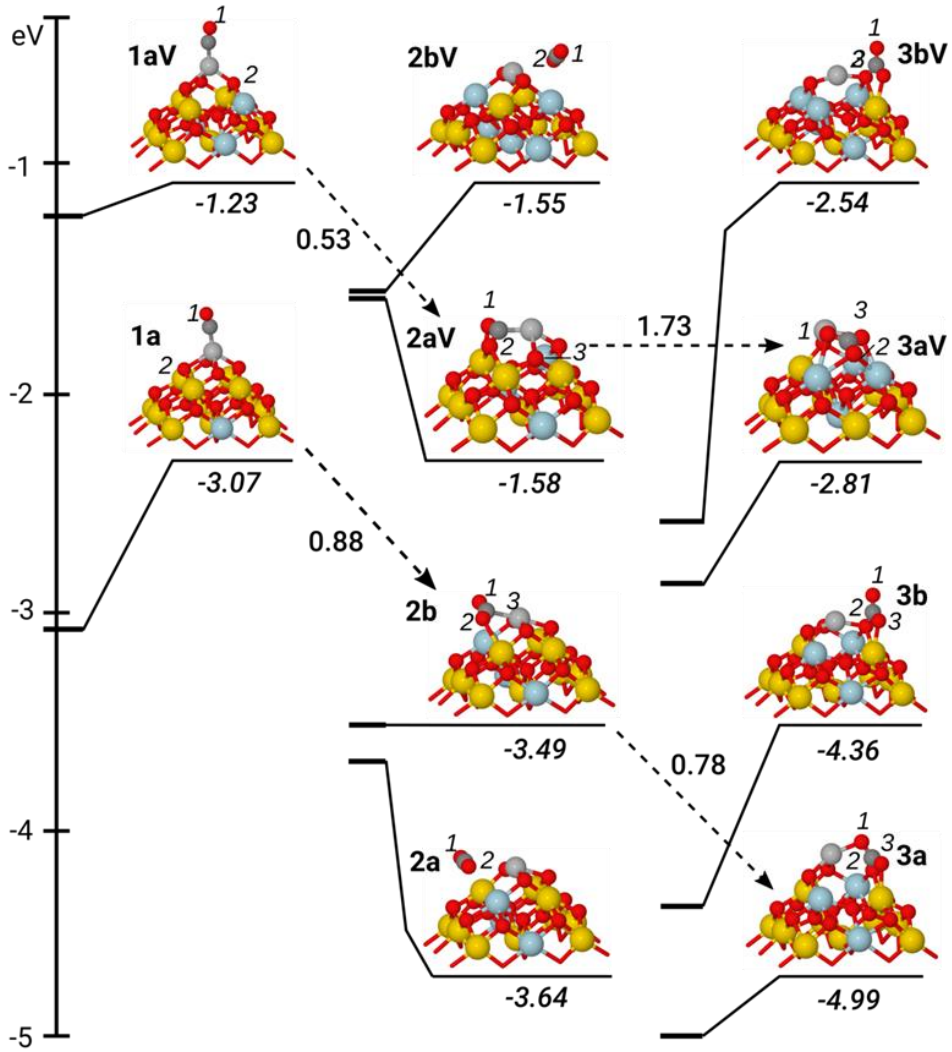


**Figure 4.** Structures and formation energies $E^f$ (in eV) of the complexes created by the interaction of CO with the $Ag/Ce_{21}O_{42-n}$ sites ($n$ = 0, 1): $AgCO/Ce_{21}O_{42}$ (**Ag1a**), $AgCO/Ce_{21}O_{41}$ (**Ag1aV**), $AgCO_2/Ce_{21}O_{41}$ (**Ag2a, Ag2b**), $AgCO_2/Ce_{21}O_{40}$ (**Ag2aV, 2bV**), $AgCO_3/Ce_{21}O_{40}$ (**Ag3a, Ag3b**) and $AgCO_3/Ce_{21}O_{39}$ (**Ag3aV, Ag3bV**). Activation energies ($E^{\neq}$) of selected transition states are shown near the dashed arrows connecting corresponding initial reagent and product. For further explanations, refer to the main text and the captions to Figures 1 and 2.

The contacts of O atoms of the $CO_2$ group with Ce atoms are ~300 pm in **2a** and 304–331 pm in **2aV** (Table 1). All attempts to locate more stable structures with a bent $CO_2$ moiety have led to carbonate moieties (described in detail in Section 3.1.4). No minima corresponding to bent $CO_2$ structures of carboxylate type were found. The only located structure with distorted $CO_2$ (**2bV** at Figure 2) was found to be 0.75 eV less stable relative to the linear **2aV** model. It features C-O bond lengths of 125 pm and an O-C-O angle of 131°. The O atoms of $CO_2$ are at 252 and 257 pm from Ce atoms. The positive $CO_2$ binding energy in **2bV** of 0.6 eV (Table 1) indicates exothermic $CO_2$ release. Since only one $Ce^{3+}$ ion is present after CO to $CO_2$ transformation, $CO_2$ in **2bV** is negatively charged, forming a $CO_2^-$ anion. Thus, $CO_2$ binds weakly and easily desorbs from bare $Ce_{21}O_{42-x}$ NP.

The metal-containing Pd/NP and Ag/NP models also feature structures with "linear" and "bent" $CO_2$ (Figures 3 and 4). Similar to the bare ceria, linear $CO_2$ is weakly bound in **Pd2b**, **Pd2bV**, **Ag2a,** and **Ag2bV**, by less than 0.2 eV (Table 1). All distances between atoms of $CO_2$ molecule and ceria are longer than 300 pm. In contrast, in "bent" $CO_2$ structures **Pd2a**, **Pd2aV**, **Ag2b,** and **Ag2aV,** $CO_2$ approaches more closely to the NP surface and forms C-M and O-Ce bonds at 193–234 and 250–270 pm, respectively. Interestingly, despite the sizable changes at the metal–adsorbate interface when going from "linear" to "bent" structures, the pairs **Ag2aV**/**Ag2bV** and **Ag2a**/**Ag2b** are isoenergetic within 0.15 eV. This observation supports our earlier finding that the formation of a new Ag-ligand bond (e.g., Ag-C with $CO_2$) does not require substantial energy (limited to 0.2 eV). The bonds of $CO_2$ in **Ag2b** are symmetrically stretched to 121 pm and the O-C-O angle is reduced to 145°, thus indicating the formation of a weakly-bound carboxylate-like complex. $CO_2$ is coordinated to Ag via the C atom at a distance of 234 pm and forms an (O)C-Ag-O angle of 175° with the Ag-O bond in trans-position. The Ag atom in $AgCO_2/Ce_{21}O_{41}$ rises above the $O_3$-plane by 52 pm (vs. 132 pm in $AgCO/Ce_{21}O_{42}$), similar to O-deficient adsorbate-free $Ag/Ce_{21}O_{41}$ complex (60 pm). Thus, the surrounding of the Ag center in **Ag2b** is nearly square-planar. The formation of the $CO_2$ moiety in **Ag2aV** does not lead to the entire detachment of the surface O* atom by adsorbed CO (Figure 4). Rather, the **Ag2aV** model can be viewed as a complex with CO inserted into the O*-Ag bond; as a result, the O*-Ag distance is stretched from 227 to 287 pm. Upon this insertion, Ce-O* bonds of the Ce-O*-Ce bridge are elongated from 218–233 pm in **Ag1aV** to 249–257 pm in **Ag2aV** (Table 1). The shortest Ce-O* distance in **Ag2b** is 268 pm. The $CO_2$ fragment in **Ag2aV** is more strongly distorted than in **Ag2b**: C-O bonds are 130 pm and the O-C-O angle is quite small, at 114°. The Ag-$CO_2$ distance (207 pm) is typical for metal–$CO_2$ complexes with an $\eta^1$-C type of $CO_2$ coordination [77]. Energies of **Ag2b** and **Ag2aV** models differ by 1.9 eV, the value close to the O vacancy formation energy at the $O_4$-pocket (Table 2).

The $PdCO_2$-containing complexes, **Pd2a** and **Pd2aV**, with a "bent" $CO_2$ moiety (Figure 3) are characterised by substantial $CO_2$ binding energies of −1.2 and −0.7 eV, respectively (Table 1). Both models exhibit a carboxylate-like structure of $CO_2$: C-O bonds are 124–130 pm long and the O-C-O angle is 130 ± 3°. In the **Pd2a** structure, $CO_2$ is $\eta^1$-coordinated to the Pd atom with the Pd-C distance, 206 pm, comparable to three Pd-O bonds around the metal center, 208–220 pm. In the **Pd2aV** complex, the $CO_2$ molecule is $\eta^2$-coordinated to Pd via the short Pd-C bond, 193 pm, and long Pd-O contact of 237 pm; two other Pd-O bond lengths are 205–220 pm. The Pd atom in both **Pd2a** and **Pd2aV** complexes is nearly in a square-planar environment with Pd shifting from the ligand plane by 25–30 pm. Interestingly, no ceria-supported $PdO_3$ structures with calculated $CO_2$ binding energies more than −0.4 eV (by module) were found in the literature [8,9,20]. The larger values −0.82 eV [20] and −0.96 eV [8] were calculated for $PdO_2$ units at $CeO_2$(110) and $CeO_2$(111) surfaces. In part, this can be explained by a favourable square-planar geometry within the $O_3Pd$-$CO_2$ fragment formed at the {100} nanofacet of $Ce_{21}O_{42}$ NP. Indeed, such structures are hindered at extended $CeO_2$ surfaces by geometrical constrains.

Thus, similar to the CO case, the strongest bonding is calculated for the $PdO_3$ site with one vacant coordination place. This is followed by the $PdO_2$ unit with two vacant valences, which binds $CO_2$ in a side-on fashion. Both structures are characterised by $CO_2$ bending.

The adsorption of $CO_2$ in linear mode results in an energy gain less than 0.2 eV for both Pd and Ag derivatives. In contrast to the Pd derivatives, both "linear" and "bent" modes have similar small adsorption energies for the Ag systems. Thus, $AgO_3$ and $AgO_2$ sites again do not show differences in adsorption properties, whereas their Pd analogs do.

#### 3.1.4. Carbonate Species

Carbonate species are formed upon the coordination of the $CO_2$ molecule via the C atom to an O center of ceria NP. Thus, $CO_3^{2-}$ formation can be considered as a form of $CO_2$ adsorption, and $CO_2$ binding energy can be applied to the estimation of the stability of these carbonate species.

The carbonate-like $CO_2$ adsorption at bare ceria NPs with binding energies of 0.84–2.22 eV (Table 1) is the most exothermic of all types of $CO_2$ coordination discussed above. The strongest binding of 2.22 eV is calculated for the tridentate 2.2.2-structure (**3aV**, Figure 2), with each O atom of the $CO_3$ moiety coordinated to two Ce ions. The flat-lying carbonate fragment of **3aV** fills two O vacancies with its oxygen atoms; i.e., all O atoms of the $CO_3$ moiety are in neighbouring O-positions of the $O_4$-pocket. The $E_b(CO_2)$ energy for **3aV** is between –1.9 and –2.3 eV, respectively, calculated for its formal 2.2.2-$CO_3$ analog on regular $CeO_2$(100) [78] and bidentate 220-$CO_3$ on O-deficient $CeO_2$(110) [74]. The 2.2.2-model features three C-O bonds equally stretched to 130 pm and O-C-O angles of 118 ± 2°. Three of four $Ce^{3+}$ ions are located in the $Ce_4$ square just below the $O_4$-pocket of the {100} nanofacet. The other tridentate 1.21-structure **3b** is stabilised by only 0.84 eV relative to the sum $CO_2$ + NP (Table 1). Here, each of the two O atoms of $CO_2$ has only one contact with Ce ions of 238 and 247 pm. As in the **3aV** model, the $CO_3$ fragment in **3b** has a slightly distorted $C_{3V}$ symmetry, with C-O bonds of 130 ± 2 pm and O-C-O angles of 117–122°. Its $CO_3$ plane is tilted by 40° relative to the $Ce_4$ layer. The $CO_2$ binding energy in the 1.21-carbonate is comparable to value −0.72 eV calculated for the flat-lying 2.21-$CO_3$ structure [71] formed upon CO adsorption at the stoichiometric $CeO_2$(100) surface with every second atom of the O layer removed. The deletion of an O atom from 1.21-**3b** to give 2.2.2-**3aV** costs only 0.67 eV. Thus, energy for the removal of a lattice O atom (~2.3 eV for formation of a 2nd O vacancy) is compensated by the formation of two new O-Ce contacts in **3aV** with ~1.6 eV energy gain. At variance, the energy difference between two 1.20-structures **3a** → **3bV**, with a bidentate coordination, 1.68 eV, does not decrease with respect to $E(O_v)$ for $Ce_{21}O_{42}$ → $Ce_{21}O_{41}$ transition, since both models have a similar bonding pattern of carbonate species. Thus, not surprisingly, the $CO_2$ binding energies for **3a** and **3bV** models are not very different, at –1.15 and −1.52 eV, respectively (Table 1). In both **3a** and **3bV** models, the $CO_3$ moiety is tied by three O-Ce bonds at 227, 238, and 245 pm. The three O-C bond lengths are different and increase from 122 to 133 and to 137 pm with the growing coordination number of O atom from 0 to 1 and to 2, respectively. Notably, at the O-deficient ceria, the flat-lying structure **3aV** is preferred over the standing one **3bV** by 0.7 eV. A similar difference of 0.84 eV was calculated for $CO_3$ moieties oriented parallel and perpendicular to the O-defective $CeO_2$ (100) facet [71]. The trend of destabilising carbonate species at ceria substrates upon surface enrichment by O atoms [71] is also supported by the present data.

Three types of carbonate structures—standing (perpendicular), tilted and flat-lying (parallel)—were also located for metal-containing ceria NPs (Figures 3 and 4). The "standing"-type carbonate species is coordinated in a bidentate way in 1.30-models **Pd3c**, **Pd3bV**, **Ag3b**, and **Ag3bV**. These structures are very similar to 1.20-carbonates **3a** and **3bV** at bare ceria NPs, with the difference that the $CO_3$ moiety is additionally bound with the M center via one short M-O bond of 211 pm (233 pm in **Ag3b**). This extra metal–oxygen bond induces the elongation of other three O-Ce contacts by 5–15 pm as well as elongates O···$CO_2$ contact by 4–9 pm, which probably weakens $CO_2$ binding from −1.15–1.52 eV in metal-free models to −0.86–1.13 and −0.39–0.50 eV in Ag- and Pd-carbonates, respectively (Table 1). Thus, for Pd-systems, carbonate-like $CO_2$ adsorption in a "standing" mode is

weaker than adsorption in carboxylate $PdCO_2$ form. Notably, Pd is in a zero-oxidation state in both types of complexes.

Stronger $CO_2$ bindings, of −1.44 and −1.40 eV, were calculated for the "flat-lying" structures 2.2.1-**Pd3a** and 2.2.2.-**Ag3aV**, respectively (Table 1). The $CO_3$ fragment is bidentately coordinated with two M-O contacts: almost equal in **Pd3a** (207 and 211 pm) and asymmetric in **Ag3aV** (216 and 265 pm). In the **Pd3a** structure, all O atoms of the $CO_3$ moiety leave their lattice positions to form short Pd-O bonds (Figure 3). This leads to the creation of a $CO_3^{2-}$ unit with a formal charge of −2 and oxidation of Pd to the +2 oxidation state. Even shorter M-O bonds are formed between metal centres and O atoms of the ceria support: 201–202 pm for Pd-O and 206 pm for Ag-O bonds. Thus, the Pd atom is four-coordinated whereas Ag is three-coordinated by O ligands. Importantly, the $PdO_4$ unit in **Pd3a** is in a slightly distorted stable square-planar configuration. Likely, this contributes greatly to making **Pd3a** the most energetically favourable among all studied ceria-supported $PdCO_x$ species. The **Pd3a** complex is even 0.25 eV more stable than another square-planar structure: carboxylate **Pd2a** complex with $O_3PdCO_2$ unit. The plane of the $CO_3$ subsystem forms a small angle of about 20° with the $O_3M$ plane. The "lying" **Ag3aV** structure is only 0.27 eV stabilised with respect to "standing" **Ag3bV,** whereas the analogous stabilisation for **Pd3a** → **Pd3c** transition reaches 0.87 eV.

The **Ag3a** 1.21-complex with the "tilted" coordination mode of $CO_3$ is the most favourable Ag-carbonate structure with a $CO_2$ adsorption energy of −1.49 eV (Table 1). Similar to the 1.30-model **Ag3b**, the $CO_2$ moiety in the **Ag3a** structure is tied in an η-C,O fashion with ceria support by means of two bonds. While the distance O-C-O···Ce is the same in **Ag3a** and **Ag3b**, the O···$CO_2$ contact in **Ag3a** is shortened to 135 pm from 141–146 pm in **Ag3b**. The shorter Ag-O contact of 221 pm (vs. 233 pm in **Ag3b**) is formed with the O atom, which has no bonds with $CeO_2$; this is comparable to the Ag-O bond length of 218 pm with ceria. Remarkably, "tilted" 1.21-complex **Ag3a** is by 0.63 eV stabilised with respect to "standing" 1.30-model **Ag3b** with an $E(CO_2)$ of −0.86 eV and reaches a $CO_2$ adsorption energy of −1.52 eV of the metal-free "standing" **3bV** model. 1.21-**Ag3a** complex has a nearly identical $CO_2$ adsorption energy (within 0.1 eV) to the "lying" 2.2.2-**Ag3aV** model. In both complexes, the cationic $Ag^+$ center is three-coordinated. Despite the closer contact of the $CO_3$ unit with ceria support in the 2.2.2-model, its formation from the **Ag3a** structure by the removal of O bound to the Ag atom requires a substantial energy of 2.18 eV. In contrast, O deletion from 1.21-**Pd3b** to give 2.2.1-**Pd3aV** is endothermic by only 1.55 eV. Both "tilted" complexes, **Pd3b** and **Pd3aV**, have $CO_2$ adsorption energies of −0.75 and −1.06 eV, respectively, bracketing the value for the "tilted" metal-free **3b** complex. Note that the **Pd3b** → **Pd3aV** transition is associated with the reduction of the Pd centre from $Pd^+$ to $Pd^0$.

In summary, carbonate $CO_3^{2-}$ species show coordination patterns different from CO and $CO_2$ moieties: they tie to the ceria support or metal centres via O atoms, whereas the C atom does not participate in adsorbate–substrate interaction. From the comparison of $CO_2$ binding energies at the metal-free and M-containing sites, it follows that $CO_2$ binds slightly more strongly in $MCO_3$/NP[0/2] structures than in $CO_3$/NP[0/2]. Conversely, the creation of an extra O vacancy stronger stabilises the formation of the carbonates at metal-free NPs than that at metal-containing NPs.

### *3.2. Reaction Energies*

In this section, we consider the energies of CO to $CO_2$ oxidation, $E^*_{ox}$, and of $CO_2$ to $CO_3$ transformation, $E^*_{CO3}$, along with the corresponding activation barriers, $E^{\neq}$, calculated for Pd/NP and Ag/NP models in comparison with the bare NP model. Data in Table 2 show that i) all these reactions are exothermic and ii) activation barriers for the carbonate formation are often higher than for the oxidation of CO.

Bare NPs adsorb CO very weakly, by less than 0.3 eV (Table 1, Figure 2). The extraction of lattice O and the formation of ceria-supported $CO_2$ yield energies of 0.9–1.4 eV and require 0.8–1.0 eV of activation (Table 2). Because of the low $CO_2$ desorption barriers,

0.15–0.25 eV (Table 1, $E_{des}(CO_2) = -E_b(CO_2)$ for **2a** and **2aV**), the formed $CO_2/Ce_{21}O_{42}$ and $CO_2/Ce_{21}O_{41}$ complexes can quite easily decompose. Otherwise, they are expected to exothermically transform into carbonates with activation barriers ranging from low—0.27 eV (for $CO_2$/NP[0/1])—to moderate—0.82 eV (for $CO_2$/NP[1/1])—values. The thermodynamic stability of such surface carbonate complexes makes them most probable candidates for experimental detection [68].

CO binds very weakly at the defect-free $PdO_4$ site of the Pd/NP[0/0] complex with an adsorption energy of −0.1 eV (**Pd1b** in Table 1). $CO_2$ can form via the interaction of the adsorbed CO with a lattice O atom. The process, which is exothermic by 1.3 eV, requires the overcoming of a barrier of 0.5 eV (Table 2). The formed $CO_2$ molecule is quite strongly bound, with a desorption energy of 1.2 eV (Table 1, $E_{des}(CO_2) = -E_b(CO_2)$ for **Pd2a**). Overcoming an even higher barrier of 1.8 eV (Table 2) is needed to extract one more lattice O centre and activate the transformation of $CO_2$ to $CO_3^{2-}$, which is exothermic by only 0.25 eV. CO is strongly, by 1.7 eV, adsorbed at the O-deficient $PdO_3$ site (**Pd1aV** in Table 1). The formed stable $O_3PdCO$ species can transform to $O_2PdCO_2$ with an activation barrier of 1.1 eV and moderate reaction exothermicity of 0.6 eV (Table 2). Slightly exothermic by 0.3 eV, the formation of carbonate is hindered by a high energy barrier of 1.8 eV. A much lower energy barrier of 0.7 eV ($-E_b(CO_2)$ for **Pd2aV** in Table 1) is required to desorb the $CO_2$ molecule into the gas phase. Thus, the most likely ceria-supported Pd-intermediates to be detected in reaction medium are saturated square-planar $O_3PdCO$/NP (**Pd1aV**) and $O_3PdCO_2$/NP (**Pd2a**) complexes whose formation proceeds with a sizable energy release (1.3–1.7 eV) and moderate activation barriers of 0.5 eV and whose decomposition is hindered by substantial barriers of about 1.1–1.2 eV.

The reactivity of Ag-containing systems is different (Table 2). CO adsorption on defect-free and O-deficient Ag/NP systems occurs with a moderate energy gain of 0.8 eV (Table 1). The formed $O_4AgCO$ and $O_3AgCO$ species are converted into the corresponding $O_3AgCO_2$ and $O_2AgCO_2$ species with a similar exothermicity around 0.4 eV, but the activation barrier for the more O-saturated complex $O_4AgCO$, 0.9 eV, is 0.4 eV higher than that for $O_3AgCO$ (Table 2). Despite the high exothermicity of 1.2–1.5 eV, the transformation to carbonates is hindered by barriers of ~0.8–1.7 eV. Alternatively, the decomposition with $CO_2$ desorption should proceed quite readily (see $-E_b(CO_2)$ values for **Ag2b** and **Ag2aV** in Table 1). Thus, the carbonyl complexes $O_4AgCO$/NP (**Ag1a**) and $O_3AgCO$ (**Ag1aV**), which are easily formed with notable energy gains, are expected to be detectable in a reaction medium. The detection of carboxylate $AgCO_2$/NP (**Ag2b** and **Ag2aV**) complexes seems problematic due to their instability with respect to $CO_2$ desorption.

We estimated the propensity of CO to $CO_2$ transformation by the energy of the CO(gas) + M/NP[$n$/0] → $CO_2$(gas) + M/NP[$n$/1] oxidation reaction, $E_{ox}$ (Equations (5) and (6)). It is directly connected with the ease of O release from the ceria lattice and O vacancy creation (Table 2).

Let us compare the oxidation reaction energy $E_{ox}$ calculated for the $O_4$-site of $CeO_2$ NP with the calculated energies for clean ceria surfaces [65,71,74,79,80] and the $Pd_1$–ceria interfaces [8,9,20]. This reaction was found to be slightly, by 0.4–0.6 eV, exothermic on bare $CeO_2$(111) [74,79] and notably more exothermic on $CeO_2$(110) [65,74,78,79], at 1.1–1.8 eV. The calculated reaction exothermicity further drastically increases to 3.1 eV for the $CeO_2$(100) surface with the most exposed O atoms [71]. Our calculated $E_{ox}$ energies for the stoichiometric and O-deficient NP{100} sites, −1.44 and −1.01 eV, respectively (Table 2), are considerably lower than those for the $CeO_2$(100) surface, but in a similar range to that for $CeO_2$(110) (assuming that the $E_{ox}$ value should increase by ca. 0.5 eV when the U value is increased from 4 to 5 eV [62]).

At the $Pd_1/CeO_2$(100) and $O_1Pd_1/CeO_2$(100) sites, the conversion of CO to $CO_2$ was characterised by energy yields of 0.6 and 1.2 eV [9], respectively—markedly lower than at the pristine $CeO_2$(100) surface. The reaction is also moderately exothermic at the $Pd_1/CeO_2$(110) interface, by 1.2 eV [20], and highly exothermic at the isolated $O_1Pd_1$ and $O_2Pd_1$ species on the $CeO_2$(111) surface, by 2.9 and 2.7 eV [8]—much more exothermic than

at the regular $CeO_2$(111) surface because of exposing weakly bonded O atoms. Compared to the above-mentioned transformations, that at Pd/NP[0/0] has the lowest $E_{ox}$ of −0.23 eV. There, the formal migration of an O-atom of the $O_4Pd$ moiety to become a part of $CO_2$ molecule is difficult even in comparison with the three-coordinated O centre of the regular $CeO_2$(111) surface. For the conversion at the Pd/NP[1/0] site with $E_{ox}$ = −1.61 eV, the relocation of the second O atom of the $O_4Pd$ moiety is more favourable than of the O atom of the isolated $O_1Pd_1$ moiety on $CeO_2$(100) or $Pd_1$ at $CeO_2$(110), but less beneficial than that of $O_1Pd_1$ or $O_2Pd_1$ ad-species on $CeO_2$(111). For the reactions on Ag/NP[$n$/0] sites, the energy $E_{ox}$, −1.0–1.2 eV, is slightly lower than on the Pd/NP[1/0] site, thus approaching $E_{ox}$ values for $O_1Pd_1/CeO_2$(100) and $Pd_1/CeO_2$(110) systems. Therefore, our model ceria particle with the Pd atom adsorbed on the O-defective {100} nanofacet appears to be more reactive in CO to $CO_2$ oxidation than its formal analogue of the Pd-doped extended $CeO_2$(100) surface.

Thus, the trend for lowering $E_{ox}$ in bare and M-containing ceria systems is Pd/NP[1/0] > NP[$n$/0] ≈ Ag/NP[$n$/0] > Pd/NP[0/0], which correlates with the growth of the O vacancy formation energy in the same row (Table 2). Note that the reactivity in CO oxidation of both Ag/NP complexes—with and without an O vacancy near the Ag atom—is similar. Conversely, the presence of an O vacancy in the vicinity of Pd atom is mandatory for CO oxidation at Pd/NP systems to proceed. This makes two consequent steps of CO oxidation at the $Pd/Ce_{21}O_{42}$ nanoparticle problematic. Such characteristics of the studied models as moderately strong CO adsorption, exothermic overall CO oxidation process, sufficiently low barriers of MCO to $MCO_2$ transformations, and ease of $CO_2$ desorption render CO oxidation by lattice ceria oxygen atoms more favourable at the sites with Ag than with Pd. Comparing the reaction and activation energies of CO to $CO_2$ and $CO_2$ to $CO_3$ conversions for M-containing ceria NPs, we conclude that the most probable species to be observed experimentally are AgCO and PdCO carbonyls and carboxylate $PdCO_2$ species. Unlike purely ceria nanoparticles, the formation of silver and palladium carbonates is prohibited by high activation barriers. We note, however, that for precise information on the species present in the reaction medium at equilibrium, a microkinetic modelling is required, which is out of the scope of the present study.

### *3.3. $CO_x$ Vibrational Fingerprints*

Several studies reported measured [7,9,16,25,26,28,68,81] and calculated [8,9,68,82–84] vibrational frequencies of CO, $CO_2$, and $CO_3^{2-}$ groups in the complexes formed by the interaction of CO or $CO_2$ with cerium-based substrates. The calculated frequencies for selected stretching vibrations of $CO_x$ subsystems of the structures displayed in Figures 2–4 are collected in Table 3.

Our modelling revealed that the CO stretching frequency, ν(CO), for the molecule attached to a cerium ion in M-free systems **1a** and **1aV** and Pd-containing model **Pd1a** shifts by 27–34 $cm^{-1}$ to the short-wave region, which agrees with the measured blue shifts of 27–32 $cm^{-1}$ (vs. 2143 $cm^{-1}$ for free molecule [85]) for CO interacting with the $Ce^{4+}$ centres of the nanostructured $CeO_2$ [19,86]. Note that the quantitatively precise reproduction of measured vibrational frequencies of CO on ceria requires going beyond the U-corrected generalised-gradient exchange-correlation functionals to hybrid-type functionals [81]. In contrast, ν(CO) for the fragments with $M_1$-CO bonding formed on M/NP[$n$/0] substrates shows redshifts of 50–113 $cm^{-1}$, consistent with the C-O bond elongation by 1–2 pm. Among the models containing $Pd_1$ species, the **Pd1b** complex with $Pd^{2+}$ cation coordinated by four two-coordinated O anions reveals a medium redshift of 84 $cm^{-1}$, and the maximum redshifts of 109–113 $cm^{-1}$ are identified for the other two complexes, **Pd1c** and **Pd1aV**, with three-fold coordinated $Pd^+$ and $Pd^{2+}$ cations (Table 3). For the earlier examined systems with Pd-CO bonds, the redshifts Δν(CO) were calculated to increase from 6 to 96 $cm^{-1}$ in the order $O_2Pd_1/CeO_2$(111) < $O_1Pd_1/CeO_2$(100) ≈ $O_1Pd_1/CeO_2$(111) < $Pd_1/CeO_2$(100) < $Pd_1/CeO_2$(111) [8,9]. These values are comparable with those attributed to the CO molecule contacting one Pd atom in experimental studies of $Pd/CeO_2$, 13–123 $cm^{-1}$ [7,28]

and 10–69 $cm^{-1}$ [9,16,25] and PdO/$CeO_2$, 58 $cm^{-1}$ [26]. Note that the Δν(CO) redshifts for CO coordinated to the supported Pd cations are opposite to the blue shift for the free $PdCO^+$ ion, measured at 63 $cm^{-1}$ and calculated at 75 $cm^{-1}$ (B3LYP), but approach a redshift for the neutral PdCO molecule, measured at 87 $cm^{-1}$ and calculated at 99 $cm^{-1}$ [70]. The redshifts of ν(CO) for **Ag1a** and **Ag1aV** complexes, at 50 and 61 $cm^{-1}$, respectively, are smaller than those for the $Pd_1$-CO moieties and correspond to about one-third of the calculated redshift for the AgCO molecule, 144 $cm^{-1}$ [87]. Similarly large frequency redshifts to those obtained for CO on single Ag and Pd cations on a ceria NP were calculated for CO adsorbed on $Pt^+$ and $Pd^{2+}$ cations anchored to ceria [83].

**Table 3.** Calculated vibrational frequencies ν(CO), ν($CO_2$) and ν($CO_3$) for the systems depicted in Figures 2–4 along with the corresponding frequency shifts Δν(CO) and Δν($CO_2$) with respect to calculated vibrational frequencies of free molecules CO (ν(free CO) = 2131 $cm^{-1}$) and $CO_2$ ($\nu_{asym}$(free $CO_2$) = 2363 $cm^{-1}$).

| System [a] | ν(CO) $cm^{-1}$ | Δν(CO) $cm^{-1}$ | ν($CO_2$) $cm^{-1}$ | Δν($CO_2$) $cm^{-1}$ | ν($CO_3$) $cm^{-1}$ |
|---|---|---|---|---|---|
| Complexes with CO | | | | | |
| **Pd1a** | 2158 | 27 | - | - | - |
| **Pd1b** | 2047 | −84 | - | - | - |
| **Pd1c** | 2022 | −109 | - | - | - |
| **Pd1aV** | 2018 | −113 | - | - | - |
| **Ag1a** | 2081 | −50 | - | - | - |
| **Ag1aV** | 2070 | −61 | - | - | - |
| **1a** | 2162 | 31 | - | - | - |
| **1aV** | 2165 | 34 | - | - | - |
| Complexes with $CO_2$ | | | | | |
| Linear O-C-O | | | | | |
| **Pd2b** | - | - | 2323 | −40 | - |
| **Pd2bV** | - | - | 2332 | −31 | - |
| **Ag2a** | - | - | 2348 | −15 | - |
| **Ag2bV** | - | - | 2350 | −13 | - |
| **2a** | - | - | 2354 | −9 | - |
| **2aV** | - | - | 2360 | −3 | - |
| **Bent O-C-O** | | | | | |
| **Pd2a** | - | - | 1535 | −828 | - |
| **Pd2aV** | - | - | 1628 | −735 | - |
| **Ag2aV** | - | - | 1332 | −1031 | - |
| **Ag2b** | - | - | 1950 | −413 | - |
| **2bV** | - | - | 1657 | −706 | - |
| Complexes with $CO_3^{2-}$ | | | | | |
| Tridentate | | | | | |
| **Pd3a** | - | - | - | - | 1573; 1221 |
| **Pd3b** | - | - | - | - | 1451; 1243 |
| **Pd3aV** | - | - | - | - | 1442; 1309 |
| **Ag3a** | - | - | - | - | 1511; 1233 |
| **Ag3aV** | - | - | - | - | 1434; 1337 |
| **3b** | - | - | - | - | 1442; 1280 |
| **3aV** | - | - | - | - | 1400; 1353 |
| **Bidentate** | | | | | |
| **Pd3c** | - | - | - | - | 1746; 1118 |
| **Pd3bV** | - | - | - | - | 1729; 1122 |
| **Ag3b** | - | - | - | - | 1689; 1126 |
| **Ag3bV** | - | - | - | - | 1752; 1169 |
| **3a** | - | - | - | - | 1714; 1082 |
| **3bV** | - | - | - | - | 1704; 1101 |

[a] For system designations see Figures 2–4.

The highest frequencies of $CO_2$ stretching vibrations in **2a**, **2aV**, **Ag2a**, **Ag2bV**, **Pd2b**, and **Pd2bV** complexes with a linear $CO_2$ moiety are close to that of the IR active $CO_2$ asymmetric stretching frequency of the free molecule; the negative shift $\Delta\nu(CO_2)$ does not exceed 40 $cm^{-1}$ (Table 3). The redshift $\Delta\nu(CO_2)$ for a bent $CO_2$ fragment in **2bV**, 706 $cm^{-1}$, is comparable to the experimental value for the free anion $CO_2^-$, 691 $cm^{-1}$ [88] (vs. measured $\nu(CO_2)$ of free molecule 2349 $cm^{-1}$ [76]) and $CO_2^-$ species at $TiO_2$ surface, 709 $cm^{-1}$ [89]. The redshift $\Delta\nu(CO_2)$ for the $MCO_2$/NP[$n$/1] systems having the M-C bond from 413 to 1031 $cm^{-1}$ is associated with the bending of the $CO_2$ moiety and C-O bond elongation by 3 to 14 pm. The redshifts for $PdCO_2$/NP systems, 828 $cm^{-1}$ (**Pd2a**) and 735 $cm^{-1}$ (**Pd2aV**), are in the range of values 610–850 $cm^{-1}$ reported for coordination compounds with $CO_2$ attached to a single d-metal atom [76], while redshift $\Delta\nu(CO_2)$ in **Ag2b** is smaller, at only 413 $cm^{-1}$. $\Delta\nu(CO_2)$ for the $CO_2^{2-}$ group in **Ag2aV** with CO bonds elongated by 14 pm compared to those of free $CO_2$ matches the measured redshifts of 1020–1079 $cm^{-1}$ for carbonite ions at $CeO_2$ [90] and in $Cs_2CO_2$ [91]. Thus, the increased redshift $\Delta\nu(CO_2)$ seems to correlate with C-O bond elongation, **Ag2b** < **Pd2aV** < **Pd2a** < **Ag2aV** (Table 1).

Differences in the length of the intramolecular C-O bonds are considered among the main factors determining the frequency splitting of $CO_3^{2-}$ stretching vibrations [68]. In tridentate $CO_3$/NP[$n$/2] and $MCO_3$/NP[$n$/2] complexes, the C-O bond lengths are 125–135 pm for the 1.11- and 1.21-modes, and in less symmetrical bidentate 1.20- and 1.30-structures, the C-O bonds cover a wider interval 121–146 pm.

Overall, the splitting of C-O frequencies is lower for more symmetrical species. In particular, for the two highest frequencies ($\nu_1$ and $\nu_2$), it is only 47 $cm^{-1}$ for 2.2.2-structures, increasing to 97–133 $cm^{-1}$ for 2.2.1-isomers and 162–252 $cm^{-1}$ for 1.2.1- and 1.1.1-isomers (Table 3). For 1.20- and 1.30-carbonates, the splitting becomes as high as 563–632 $cm^{-1}$. According to earlier calculations, carbonate groups attached to nanostructured ceria surface by three oxygen atoms, represented by sets of 1.21-, 1.2.1- and 1.3.1-structures, are characterised by $\nu_1$ values from 1590 to 1490 $cm^{-1}$ [68]. With the inclusion of $\nu_1$ values for tridentate structures **3b** and **3aV**, this range extends to 1400 $cm^{-1}$. The calculated $\nu_1$ for tridentate carbonates corresponds to a broad experimental region of 1620–1450 $cm^{-1}$ attributed to the high-frequency vibrations of the carbonate groups formed on surfaces with oxygen vacancies, as well as on facet, edge, and corner sites of ceria particles [68]. The $\nu_1$ frequencies for tridentate carbonate **Ag3a**, **Pd3a**, **Pd3b**, **Ag3aV**, and **Pd3aV** complexes, of 1573–1434 $cm^{-1}$, fall between the limits of the clean surface of the nanostructured ceria. The $\nu_1$ values for 1.20-carbonate groups in **3a** and **3bV** systems are in a narrow range of 1718–1698 $cm^{-1}$ for bidentate carbonates [68] corresponding to the measured frequency interval of 1732–1722 $cm^{-1}$ [68]. The $\nu_1$ frequencies of the M-containing 1.30-complexes **Pd3c, Pd3bV, Ag3b,** and **Ag3bV** are in a broader range of 1752–1689 $cm^{-1}$, which includes the interval for bidentate $CO_3^{2-}$ on M-free ceria substrates.

The calculated $\nu_2$ frequency range of the complexes on the clean ceria surface is 1353–1227 $cm^{-1}$. This corresponds to the experimental frequencies of 1380 and 1280 $cm^{-1}$ [68]. The $\nu_2$ values for tridentate 1.21- and 2.2.1-carbonates **P3b, Pd3aV, Ag3a,** and **Ag3aV** for M-containing systems, at 1340–1220 $cm^{-1}$, are between these limits, and that for the 1.11-**Pd3a** isomer is only 6 $cm^{-1}$ below the low-end threshold. The $\nu_2$ frequencies are distributed between 1194 and 1082 $cm^{-1}$ for bidentate carbonates depicted in Figure 2 and those examined in [68]; the related experimental values are 1147–1133 $cm^{-1}$ [68].

The range of $\nu_2$ for the $CO_3$ moieties coordinated in a bidentate way at M/NP systems is 1170–1120 $cm^{-1}$. Thus, the frequency ranges are similar for the metal-free $CO_3$/NP and $MCO_3$/NP sites, making the discrimination between the metal-containing and bare ceria particles solely on the basis of the vibrational spectroscopy data problematic.

In summary, our calculations show that the C-O stretching vibrations of the ceria-supported PdCO and AgCO fragments feature redshifts up to ~110 $cm^{-1}$, which is at variance with the blue shift at metal-free ceria. Redshifts of $CO_2$ asymmetric stretching frequency of the M-$CO_2$ fragments are much higher, up to ~830 $cm^{-1}$ for carboxy-

late $MCO_2$ and further increasing by ~200 $cm^{-1}$ for carbonite $AgCO_2$. The two highest $\nu(CO_3)$ stretching frequencies of M-$CO_3$ structures lie in intervals 1755–1690 $cm^{-1}$ and 1170–1120 $cm^{-1}$ for the $CO_3$ moiety coordinated in a bidentate fashion and 1575–1430 $cm^{-1}$ and 1340–1220 $cm^{-1}$ for the $CO_3$ in the tridentate coordination.

## 4. Conclusions

$CO_x$ intermediates formed upon CO adsorption and oxidation on single M = Pd and Ag atoms coordinated to the $O_4$-site on the {100} facet of a $Ce_{21}O_{42}$ nanoparticle have been studied computationally. Equilibrium structures, $CO_x$ vibrational frequencies, and energetic parameters of various $MCO_x$-containing complexes have been determined. The influence of the creation of an O vacancy nearby the M atom has been also investigated. The stability of the $CO_x$ moieties anchored to the ceria-supported M atom is found to increase in the order MCO < $MCO_2$ < $MCO_3$, similar to the trend for $CO_x$ species adsorbed on M-free ceria NP.

Except for the Pd atom saturated by four O atoms of the ceria surface $O_4$-site, which is unable to properly adsorb CO, the doping of the ceria nanoparticle with Pd and Ag atom increases its propensity to bind the CO molecule with respect to bare ceria material. In particular, the CO adsorption energy value reaches −1.7 eV for a PdCO unit on a ceria nanoparticle with a nearby O vacancy. CO binding in AgCO complexes, regardless of the presence or absence of a nearby O vacancy, is moderately strong, at −0.8 eV. All these species are the most probable candidates to be detected experimentally, also due to the presence of moderate barriers for CO oxidation (0.5–1.0 eV). In contrast to the blue shift for CO adsorbed on pristine ceria, red shifts of the C-O stretching (vs. free CO) have been calculated for MCO species anchored to ceria. The red shifts of the CO stretching frequency are higher for complexes of Pd and increase with the decreasing coordination of M from $MO_4$ to $MO_3$ for a particular metal: $Ag/Ce_{21}O_{42}$ (50 $cm^{-1}$) < $Ag/Ce_{21}O_{41}$ (61 $cm^{-1}$) < $Pd/Ce_{21}O_{42}$ (84 $cm^{-1}$) < $Pd/Ce_{21}O_{41}$ (113 $cm^{-1}$).

Carboxylate $CO_2^-$ and carbonite $CO_2^{2-}$ (for Ag-doped NP with an O vacancy) complexes featuring a bent $CO_2$ moiety are formed upon CO oxidation at the M/ceria interface. Contrary to $AgCO_2$-species, which are easily decomposed via $CO_2$ detachment, $PdCO_2$ moieties are prone to withstand decomposition due to significant $CO_2$ desorption energies of 0.7–1.2 eV. These $PdCO_2$ moieties anchored to ceria particles could be experimentally detected by the red shifts of the $CO_2$ asymmetric stretching frequency (vs. that of free $CO_2$ molecule) by 828 $cm^{-1}$ (one O vacancy nearby Pd) and 735 $cm^{-1}$ (two O vacancies nearby Pd).

Unlike pristine ceria, carbonate structures at ceria-supported Pd and Ag atoms are hardly formed before $CO_2$ desorption due to the high barriers of $CO_2$ transformation to $CO_3^{2-}$ (up to 1.8 eV for $PdCO_3$ moieties) and weak $CO_2$ binding (below ~0.2 eV for $AgCO_3$ moieties). Detailed analysis of the vibrational spectra of $MCO_3$/NP complexes has shown that the two highest $\nu(CO_3)$ stretching frequencies lie in the well-resolved intervals 1755–1690 and 1170–1120 $cm^{-1}$ for the $CO_3$ moiety coordinated in a bidentate fashion and 1575–1430 and 1340–1220 $cm^{-1}$ for the carbonate groups in the tridentate coordination. These frequency ranges are similar to those for the M-free $CO_3$/NP sites. Thus, discrimination between the M-containing and bare ceria particles solely using vibrational spectroscopy data seems hardly possible.

In summary, such characteristics of the studied models as moderately strong CO adsorption, an exothermic CO oxidation process, sufficiently low barriers of MCO to $MCO_2$ transformations, and ease of $CO_2$ desorption render CO oxidation by lattice ceria oxygen atoms more favourable at the sites with Ag than with Pd.

**Supplementary Materials:** The following data are available online at https://www.mdpi.com/article/10.3390/ma14226888/s1: Coordinates of the atomic positions of all considered $Ce_{21}O_{42-\delta}$, $CO_x/Ce_{21}O_{42-\delta}$, $AgCO_x/Ce_{21}O_{42-\delta}$ and $PdCO_x/Ce_{21}O_{42-\delta}$ complexes and selected transition state structures connecting these complexes along with their total energies.

**Author Contributions:** Conceptualisation, V.A.N., E.A.I.-S. and K.M.N.; methodology, V.A.N. and E.A.I.-S.; software, V.A.N. and S.S.L.; investigation, V.A.N. and S.S.L.; validation, V.A.N. and E.A.I.-S.; formal analysis, V.A.N., A.M.S. and E.A.I.-S.; resources, V.A.N. and E.A.I.-S.; data curation, V.A.N.; writing—original draft preparation, V.A.N., E.A.I.-S. and K.M.N.; writing—review and editing, V.A.N., E.A.I.-S., A.M.S., S.S.L. and K.M.N.; visualisation, V.A.N. and A.M.S.; supervision, V.A.N., E.A.I.-S. and K.M.N. All authors have read and agreed to the published version of the manuscript.

**Funding:** This work was conducted within the framework of the budget project No. 0287-2021-0012 for Institute of Chemistry and Chemical Technology SB RAS. The work of K.M.N. was funded by the Spanish Government MCIN/AEI/10.13039/501100011033 via grants PGC2018-093863-B-C22, MDM-2017-0767 and PRX17/00348 as well as by the grant 2017SGR13 of the Generalitat de Catalunya.

**Institutional Review Board Statement:** Not applicable.

**Informed Consent Statement:** Not applicable.

**Data Availability Statement:** Data is contained within the article or Supplementary Material.

**Acknowledgments:** The authors thank the Supercomputer Center of the Institute of Computational Modeling SB RAS for providing computational resources. K.M.N. thanks the European Cooperation in Science and Technology program via the COST Action 18234.

**Conflicts of Interest:** The authors declare no conflict of interest.

## References

1. Grabchenko, M.V.; Mikheeva, N.N.; Mamontov, G.V.; Salaev, M.A.; Liotta, L.F.; Vodyankina, O.V. Ag/$CeO_2$ Composites for Catalytic Abatement of CO, Soot and VOCs. *Catalysts* **2018**, *8*, 285. [CrossRef]
2. Grabchenko, M.V.; Mamontov, G.V.; Zaikovskii, V.I.; La Parola, V.; Liotta, L.F.; Vodyankina, O.V. The Role of Metal–Support Interaction in Ag/$CeO_2$ Catalysts for CO and Soot Oxidation. *Appl. Catal. B Environ.* **2020**, *260*, 118148. [CrossRef]
3. Shimizu, K.; Kawachi, H.; Satsuma, A. Study of Active Sites and Mechanism for Soot Oxidation by Silver-Loaded Ceria Catalyst. *Appl. Catal. B* **2010**, *96*, 169–175. [CrossRef]
4. Bera, P.; Patil, K.C.; Hegde, M.S. NO Reduction, CO and Hydrocarbon Oxidation over Combustion Synthesized Ag/$CeO_2$ Catalyst. *Phys. Chem. Chem. Phys.* **2000**, *2*, 3715–3719. [CrossRef]
5. Tan, H.; Wang, J.; Yu, S.; Zhou, K. Support Morphology-Dependent Catalytic Activity of Pd/$CeO_2$ for Formaldehyde Oxidation. *Environ. Sci. Technol.* **2015**, *49*, 8675–8682. [CrossRef]
6. Colussi, S.; Gayen, A.; Camellone, M.F.; Boaro, M.; Llorca, J.; Fabris, S.; Trovarelli, A. Nanofaceted Pd-O Sites in Pd-Ce Surface Superstructures: Enhanced Activity in Catalytic Combustion of Methane. *Angew. Chem. Int. Ed.* **2009**, *48*, 8481–8484. [CrossRef] [PubMed]
7. Boronin, A.I.; Slavinskaya, E.M.; Danilova, I.G.; Gulyaev, R.V.; Amosov, Y.u.I.; Kuznetsov, P.A.; Polukhina, I.A.; Koscheev, S.V.; Zaikovskii, V.I.; Noskov, A.S. Investigation of Palladium Interaction with Cerium Oxide and Its State in Catalysts for Low-Temperature CO Oxidation. *Catal. Today* **2009**, *144*, 201–211. [CrossRef]
8. Spezzati, G.; Su, Y.; Hofmann, J.P.; Benavidez, A.D.; DeLaRiva, A.T.; McCabe, J.; Datye, A.K.; Hensen, E.J.M. Atomically Dispersed Pd–O Species on $CeO_2$(111) as Highly Active Sites for Low-Temperature CO Oxidation. *ACS Catal.* **2017**, *7*, 6887–6891. [CrossRef]
9. Spezzati, G.; Benavidez, A.D.; DeLaRiva, A.T.; Su, Y.; Hofmann, J.P.; Asahina, S.; Olivier, E.J.; Neethling, J.H.; Miller, J.T.; Datye, A.K.; et al. CO Oxidation by Pd Supported on $CeO_2$(100) and $CeO_2$(111) Facets. *Appl. Catal. B* **2019**, *243*, 36–46. [CrossRef]
10. Wang, J.; Chen, H.; Hu, Z.; Yao, M.; Li, Y. A Review on the Pd-Based Three-Way Catalyst. *Catal. Rev.* **2015**, *57*, 79–144. [CrossRef]
11. Carraro, F.; Fapohunda, A.; Paganini, M.C.; Agnoli, S. Morphology and Size Effect of Ceria Nanostructures on the Catalytic Performances of Pd/$CeO_2$ Catalysts for Methanol Decomposition to Syngas. *ACS Appl. Nano Mater.* **2018**, *1*, 1492–1501. [CrossRef]
12. Fan, L.; Fujimoto, K. Reaction Mechanism of Methanol Synthesis from Carbon Dioxide and Hydrogen on Ceria-Supported Palladium Catalysts with SMSI Effect. *J. Catal.* **1997**, *172*, 238–242. [CrossRef]
13. Guo, C.; Wei, S.; Zhou, S.; Zhang, T.; Wang, Z.; Ng, S.-P.; Lu, X.; Wu, C.-M.L.; Guo, W. Initial Reduction of $CO_2$ on Pd-, Ru-, and Cu-Doped $CeO_2$(111) Surfaces: Effects of Surface Modification on Catalytic Activity and Selectivity. *ACS Appl. Mater. Interfaces* **2017**, *9*, 26107–26117. [CrossRef]
14. Farmer, J.A.; Campbell, C.T. Ceria Maintains Smaller Metal Catalyst Particles by Strong Metal-Support Bonding. *Science* **2010**, *329*, 933–936. [CrossRef]
15. Lykhach, Y.; Kozlov, S.M.; Skála, T.; Tovt, A.; Stetsovych, V.; Tsud, N.; Dvořák, F.; Johánek, V.; Neitzel, A.; Mysliveček, J.; et al. Counting Electrons on Supported Nanoparticles. *Nat. Mater.* **2016**, *15*, 284–288. [CrossRef]
16. You, R.; Li, Z.; Cao, T.; Nan, B.; Si, R.; Huang, W. Synthesis in a Glovebox: Utilizing Surface Oxygen Vacancies To Enhance the Atomic Dispersion of Palladium on Ceria for Carbon Monoxide Oxidation and Propane Combustion. *ACS Appl. Nano Mater.* **2018**, *1*, 4988–4997. [CrossRef]

17. Boronin, A.I.; Slavinskaya, E.M.; Figueroba, A.; Stadnichenko, A.I.; Kardash, T.Y.; Stonkus, O.A.; Fedorova, E.A.; Muravev, V.V.; Svetlichnyi, V.A.; Bruix, A.; et al. CO Oxidation Activity of Pt/$CeO_2$ Catalysts Below 0 °C: Platinum Loading Effects. *Appl. Catal. B Environ.* **2021**, *286*, 119931. [CrossRef]
18. Pentyala, P.; Deshpande, P.A. CO Oxidation over $Ce_{1-x}Pd_xO_{2-\delta}$ Takes Place via Vacancy Hopping. *Ind. Eng. Chem. Res.* **2019**, *58*, 7964–7972. [CrossRef]
19. Wu, Z.; Li, M.; Overbury, S.H. On the Structure Dependence of CO Oxidation over $CeO_2$ nanocrystals with well-defined surface planes. *J. Catal.* **2012**, *285*, 61–73. [CrossRef]
20. Song, W.; Su, Y.; Hensen, E.J.M. A DFT Study of CO Oxidation at the Pd–$CeO_2$(110) Interface. *J. Phys. Chem. C* **2015**, *119*, 27505–27511. [CrossRef]
21. Groppi, G.; Cristiani, C.; Lietti, L.; Ramella, C.; Valentini, M.; Forzatti, P. Effect of Ceria on Palladium Supported Catalysts for High Temperature Combustion of $CH_4$ under Lean Conditions. *Catal. Today* **1999**, *50*, 399–412. [CrossRef]
22. Sharma, S.; Hilaire, S.; Vohs, J.M.; Gorte, R.J.; Jen, H.-W. Evidence for Oxidation of Ceria by $CO_2$. *J. Catal.* **2000**, *190*, 199–204. [CrossRef]
23. Scanlon, D.O.; Morgan, B.J.; Watson, G.W. The Origin of the Enhanced Oxygen Storage Capacity of $Ce_{1-x}(Pd/Pt)_xO_2$. *Phys. Chem. Chem. Phys.* **2011**, *13*, 4279. [CrossRef]
24. Chang, S.; Li, M.; Hua, Q.; Zhang, L.; Ma, Y.; Ye, B.; Huang, W. Shape-Dependent Interplay between Oxygen Vacancies and Ag–$CeO_2$ Interaction in Ag/$CeO_2$ Catalysts and Their Influence on the Catalytic Activity. *J. Catal.* **2012**, *293*, 195–204. [CrossRef]
25. Hu, Z.; Liu, X.; Meng, D.; Guo, Y.; Guo, Y.; Lu, G. Effect of Ceria Crystal Plane on the Physicochemical and Catalytic Properties of Pd/Ceria for CO and Propane Oxidation. *ACS Catal.* **2016**, *6*, 2265–2279. [CrossRef]
26. Meng, L.; Jia, A.-P.; Lu, J.-Q.; Luo, L.-F.; Huang, W.-X.; Luo, M.-F. Synergetic Effects of PdO Species on CO Oxidation over PdO–$CeO_2$ Catalysts. *J. Phys. Chem. C* **2011**, *115*, 19789–19796. [CrossRef]
27. Gulyaev, R.V.; Kardash, T.Y.; Malykhin, S.E.; Stonkus, O.A.; Ivanova, A.S.; Boronin, A.I. The Local Structure of $Pd_xCe_{1-x}O_{2-x-\delta}$ Solid Solutions. *Phys. Chem. Chem. Phys.* **2014**, *16*, 13523–13539. [CrossRef]
28. Craciun, R.; Daniell, W.; Knözinger, H. The Effect of $CeO_2$ Structure on the Activity of Supported Pd Catalysts Used for Methane Steam Reforming. *Appl. Catal. A* **2002**, *230*, 153–168. [CrossRef]
29. Luches, P.; Pagliuca, F.; Valeri, S.; Illas, F.; Preda, G.; Pacchioni, G. Nature of Ag Islands and Nanoparticles on the $CeO_2$(111) Surface. *J. Phys. Chem. C* **2012**, *116*, 1122–1132. [CrossRef]
30. Liu, J.-X.; Su, Y.; Filot, I.A.W.; Hensen, E.J.M. A Linear Scaling Relation for CO Oxidation on $CeO_2$-Supported Pd. *J. Am. Chem. Soc.* **2018**, *140*, 4580–4587. [CrossRef]
31. Shen, M.; Wei, G.; Yang, H.; Wang, J.; Wang, X. Different Selections of Active Sites for CO, $C_3H_6$, and $C_{10}H_{22}$ Oxidation on Pd/$CeO_2$ Catalysts. *Fuel* **2013**, *103*, 869–875. [CrossRef]
32. Hiley, C.I.; Fisher, J.M.; Thompsett, D.; Kashtiban, R.J.; Sloan, J.; Walton, R.I. Incorporation of Square-Planar $Pd^{2+}$ in Fluorite $CeO_2$: Hydrothermal Preparation, Local Structure, Redox Properties and Stability. *J. Mater. Chem. A* **2015**, *3*, 13072–13079. [CrossRef]
33. Su, Y.-Q.; Filot, I.A.W.; Liu, J.-X.; Hensen, E.J.M. Stable Pd-Doped Ceria Structures for $CH_4$ Activation and CO Oxidation. *ACS Catal.* **2018**, *8*, 75–80. [CrossRef]
34. Priolkar, K.R.; Bera, P.; Sarode, P.R.; Hegde, M.S.; Emura, S.; Kumashiro, R.; Lalla, N.P. Formation of $Ce_{1-x}Pd_xO_{2-\delta}$ Solid Solution in Combustion-Synthesized Pd/$CeO_2$ Catalyst: XRD, XPS, and EXAFS Investigation. *Chem. Mat.* **2002**, *14*, 2120–2128. [CrossRef]
35. Figueroba, A.; Bruix, A.; Kovács, G.; Neyman, K.M. Metal-Doped Ceria Nanoparticles: Stability and Redox Processes. *Phys. Chem. Chem. Phys.* **2017**, *19*, 21729–21738. [CrossRef]
36. Neitzel, A.; Figueroba, A.; Lykhach, Y.; Skála, T.; Vorokhta, M.; Tsud, N.; Mehl, S.; Ševčíková, K.; Prince, K.C.; Neyman, K.M.; et al. Atomically Dispersed Pd, Ni, and Pt Species in Ceria-Based Catalysts: Principal Differences in Stability and Reactivity. *J. Phys. Chem. C* **2016**, *120*, 9852–9862. [CrossRef]
37. Figueroba, A.; Kovács, G.; Bruix, A.; Neyman, K.M. Towards Stable Single-Atom Catalysts: Strong Binding of Atomically Dispersed Transition Metals on the Surface of Nanostructured Ceria. *Catal. Sci. Technol.* **2016**, *6*, 6806–6813. [CrossRef]
38. Nasluzov, V.A.; Ivanova-Shor, E.A.; Shor, A.M.; Neyman, K.M. Silver Atom, Trimer and Tetramer Species Supported on a Ceria Nanoparticle: A Density Functional Study. *Surf. Sci.* **2019**, *681*, 38–46. [CrossRef]
39. Li, L.; Chang, X.; Lin, X.; Zhao, Z.-J.; Gong, J. Theoretical Insights into Single-Atom Catalysts. *Chem. Soc. Rev.* **2020**, *49*, 8156–8178. [CrossRef]
40. Ding, W.-C.; Gu, X.-K.; Su, H.-Y.; Li, W.-X. Single Pd Atom Embedded in $CeO_2$(111) for NO Reduction with CO: A First-Principles Study. *J. Phys. Chem. C* **2014**, *118*, 12216–12223. [CrossRef]
41. Nasluzov, V.A.; Neyman, K.M.; Shor, A.M.; Laletina, S.S.; Ivanova-Shor, E.A. Density Functional Calculation of Dioxygen Adsorption at Complexes of Ceria Nanoparticle with Atoms, Trimers and Tetramers of Silver. *J. Sib. Fed. Univ. Chem.* **2016**, *3*, 281–295. [CrossRef]
42. Preda, G.; Pacchioni, G. Formation of oxygen active species in Ag-modified $CeO_2$ catalyst for soot oxidation: A DFT study, Catal. *Today* **2011**, *177*, 31–38. [CrossRef]
43. Brugnoli, L.; Pedone, A.; Menziani, M.C.; Adamo, C.; Labat, F. $O_2$ Activation over Ag-Decorated $CeO_2$ (111) and $TiO_2$ (110) Surfaces: A Theoretical Comparative Investigation. *J. Phys. Chem. C* **2020**, *124*, 25917–25930. [CrossRef]
44. Bromley, S.T.; de Moreira I, P.R.; Neyman, K.M.; Illas, F. Approaching Nanoscale Oxides: Models and Theoretical Methods. *Chem. Soc. Rev.* **2009**, *38*, 2657. [CrossRef] [PubMed]

45. Bruix, A.; Neyman, K.M. Modeling Ceria-Based Nanomaterials for Catalysis and Related Applications. *Catal. Lett.* **2016**, *146*, 2053–2080. [CrossRef]
46. Loschen, C.; Migani, A.; Bromley, S.T.; Illas, F.; Neyman, K.M. Density Functional Studies of Model Cerium Oxide Nanoparticles. *Phys. Chem. Chem. Phys.* **2008**, *10*, 5730–5738. [CrossRef]
47. Migani, A.; Vayssilov, G.N.; Bromley, S.T.; Illas, F.; Neyman, K.M. Greatly Facilitated Oxygen Vacancy Formation in Ceria Nanocrystallites. *Chem. Comm.* **2010**, *46*, 5936. [CrossRef]
48. Bruix, A.; Neyman, K.M. How to design models for ceria nanoparticles: Challenges and strategies for describing nanostructured reducible oxides. In *Computational Modelling of Nanoparticles, Frontiers of Nanoscience*; Bromley, S.T., Woodley, S.M., Eds.; Elsevier: Oxford, UK, 2018; Volume 12, pp. 55–99, ISBN 978-0-08-102232-0.
49. Bruix, A.; Lykhach, Y.; Matolínová, I.; Neitzel, A.; Skála, T.; Tsud, N.; Vorokhta, M.; Stetsovych, V.; Ševčíková, K.; Mysliveček, J.; et al. Maximum Noble-Metal Efficiency in Catalytic Materials: Atomically Dispersed Surface Platinum. *Angew. Chem. Int. Ed.* **2014**, *53*, 10525–10530. [CrossRef]
50. Aleksandrov, H.A.; Neyman, K.M.; Vayssilov, G.N. The Structure and Stability of Reduced and Oxidized Mononuclear Platinum Species on Nanostructured Ceria from Density Functional Modeling. *Phys. Chem. Chem. Phys.* **2015**, *17*, 14551–14560. [CrossRef]
51. Koleva, I.Z.; Aleksandrov, H.A.; Vayssilov, G.N. Decomposition Behavior of Platinum Clusters Supported on Ceria and γ-Alumina in the Presence of Carbon Monoxide. *Catal. Sci. Technol.* **2017**, *7*, 734–742. [CrossRef]
52. Kresse, G.; Hafner, J. Ab Initio Molecular Dynamics for Liquid Metals. *Phys. Rev. B* **1993**, *47*, 558–561. [CrossRef]
53. Kresse, G.; Furthmüller, J. Efficient Iterative Schemes for Ab Initio Total-Energy Calculations Using a Plane-Wave Basis Set. *Phys. Rev. B* **1996**, *54*, 11169–11186. [CrossRef] [PubMed]
54. Blöchl, P.E. Projector Augmented-Wave Method. *Phys. Rev. B* **1994**, *50*, 17953–17979. [CrossRef] [PubMed]
55. Kresse, G.; Joubert, D. From Ultrasoft Pseudopotentials to the Projector Augmented-Wave Method. *Phys. Rev. B* **1999**, *59*, 1758–1775. [CrossRef]
56. Viñes, F.; Illas, F.; Neyman, K.M. On the Mechanism of Formation of Metal Nanowires by Self-Assembly. *Angew. Chem. Int. Ed.* **2007**, *46*, 7094–7097. [CrossRef] [PubMed]
57. Sk, M.A.; Kozlov, S.M.; Lim, K.H.; Migani, A.; Neyman, K.M. Oxygen Vacancies in Self-Assemblies of Ceria Nanoparticles. *J. Mater. Chem. A* **2014**, *2*, 18329–18338. [CrossRef]
58. Perdew, J.P.; Chevary, J.A.; Vosko, S.H.; Jackson, K.A.; Pederson, M.R.; Singh, D.J.; Fiolhais, C. Atoms, Molecules, Solids, and Surfaces: Applications of the Generalized Gradient Approximation for Exchange and Correlation. *Phys. Rev. B* **1992**, *46*, 6671–6687, Erratum in **1993**, *48*, 4978–4978. [CrossRef]
59. Rohrbach, A.; Hafner, J.; Kresse, G. Electronic Correlation Effects in Transition-Metal Sulfides. *J. Phys. Condens. Matter* **2003**, *15*, 979–996. [CrossRef]
60. Dudarev, S.L.; Savrasov, S.Y.; Humphreys, C.J.; Sutton, A.P. Electron-Energy-Loss Spectra and the Structural Stability of Nickel Oxide: An LSDA+U Study. *Phys. Rev. B* **1998**, *57*, 1505–1509. [CrossRef]
61. Loschen, C.; Carrasco, J.; Neyman, K.; Illas, F. First-Principles LDA+U and GGA+U Study of Cerium Oxides: Dependence on the Effective U Parameter. *Phys. Rev. B* **2007**, *75*, 035117. [CrossRef]
62. Bennett, L.J.; Jones, G. The Influence of the Hubbard U Parameter in Simulating the Catalytic Behaviour of Cerium Oxide. *Phys. Chem. Chem. Phys.* **2014**, *16*, 21032–21038. [CrossRef]
63. Vayssilov, G.N.; Migani, A.; Neyman, K. Density Functional Modeling of the Interactions of Platinum Clusters with $CeO_2$ Nanoparticles of Different Size. *J. Phys. Chem. C* **2011**, *115*, 16081–16086. [CrossRef]
64. Bruix, A.; Migani, A.; Vayssilov, G.N.; Neyman, K.M.; Libuda, J.; Illas, F. Effects of Deposited Pt Particles on the Reducibility of $CeO_2$(111). *Phys. Chem. Chem. Phys.* **2011**, *13*, 11384. [CrossRef] [PubMed]
65. Huang, M.; Fabris, S. CO Adsorption and Oxidation on Ceria Surfaces from DFT+U Calculations. *J. Phys. Chem. C* **2008**, *112*, 8643–8648. [CrossRef]
66. Weinan, E.; Ren, W.; Vanden-Eijnden, E. String Method for the Study of Rare Events. *Phys. Rev. B* **2002**, *66*, 052301. [CrossRef]
67. Chaffey-Millar, H.; Nikodem, A.; Matveev, A.V.; Krüger, S.; Rösch, N. Improving Upon String Methods for Transition State Discovery. *J. Chem. Theor. Comput.* **2012**, *8*, 777–786. [CrossRef] [PubMed]
68. Vayssilov, G.N.; Mihaylov, M.; Petkov, P.S.; Hadjiivanov, K.I.; Neyman, K.M. Reassignment of the Vibrational Spectra of Carbonates, Formates, and Related Surface Species on Ceria: A Combined Density Functional and Infrared Spectroscopy Investigation. *J. Phys. Chem. C* **2011**, *115*, 23435–23454. [CrossRef]
69. Hulva, J.; Meier, M.; Bliem, R.; Jakub, Z.; Kraushofer, F.; Schmid, M.; Diebold, U.; Franchini, C.; Parkinson, G.S. Unraveling CO Adsorption on Model Single-atom Catalysts. *Science* **2021**, *371*, 375–379. [CrossRef]
70. Liang, B.; Zhou, M.; Andrews, L. Reactions of Laser-Ablated Ni, Pd, and Pt Atoms with Carbon Monoxide: Matrix Infra-red Spectra and Density Functional Calculations on $M(CO)_n$ (n = 1−4), $M(CO)_n^-$ (n = 1−3), and $M(CO)_n^+$ (n = 1−2), (M = Ni, Pd, Pt). *J. Phys. Chem. A* **2000**, *104*, 3905–3914. [CrossRef]
71. Zhong, S.-H.; Lu, G.; Gong, X.-Q. A DFT+U Study of the Structures and Reactivities of Polar $CeO_2$(100) Surfaces. *Chinese J. Catal.* **2017**, *38*, 1138–1147. [CrossRef]
72. Kumari, N.; Haider, M.A.; Agarwal, M.; Sinha, N.; Basu, S. Role of Reduced $CeO_2$(110) Surface for $CO_2$ Reduction to CO and Methanol. *J. Phys. Chem. C* **2016**, *120*, 16626–16635. [CrossRef]

73. Hahn, K.R.; Iannuzzi, M.; Seitsonen, A.P.; Hutter, J. Coverage Effect of the $CO_2$ Adsorption Mechanisms on $CeO_2$(111) by First Principles Analysis. *J. Phys. Chem. C* **2013**, *117*, 1701–1711. [CrossRef]
74. Chen, F.; Liu, D.; Zhang, J.; Hu, P.; Gong, X.-Q.; Lu, G. A DFT+U Study of the Lattice Oxygen Reactivity toward Direct CO Oxidation on the $CeO_2$(111) and (110) Surfaces. *Phys. Chem. Chem. Phys.* **2012**, *14*, 16573. [CrossRef] [PubMed]
75. Cheng, Z.; Sherman, B.J.; Lo, C.S. Carbon Dioxide Activation and Dissociation on Ceria (110): A Density Functional Theory Study. *J. Chem. Phys.* **2013**, *138*, 014702. [CrossRef] [PubMed]
76. Lu, X.; Wang, W.; Wei, S.; Guo, C.; Shao, Y.; Zhang, M.; Deng, Z.; Zhu, H.; Guo, W. Initial Reduction of $CO_2$ on Perfect and O-Defective $CeO_2$(111) Surfaces: Towards CO or COOH? *RSC Adv.* **2015**, *5*, 97528–97535. [CrossRef]
77. Gibson, D.H. Carbon Dioxide Coordination Chemistry: Metal Complexes and Surface-Bound Species. What Relationships? *Coord. Chem. Rev.* **1999**, *185–186*, 335–355. [CrossRef]
78. Albrecht, P.M.; Jiang, D.; Mullins, D.R. $CO_2$ Adsorption As a Flat-Lying, Tridentate Carbonate on $CeO_2$(100). *J. Phys. Chem. C* **2014**, *118*, 9042–9050. [CrossRef]
79. Scanlon, D.O.; Galea, N.M.; Morgan, B.J.; Watson, G.W. Reactivity on the (110) Surface of Ceria: A GGA+U Study of Surface Reduction and the Adsorption of CO and $NO_2$. *J. Phys. Chem. C* **2009**, *113*, 11095–11103. [CrossRef]
80. Nolan, M.; Parker, S.C.; Watson, G.W. $CeO_2$ Catalysed Conversion of CO, $NO_2$ and NO from First Principles Energetics. *Phys. Chem. Chem. Phys.* **2006**, *8*, 216. [CrossRef]
81. Binet, C.; Daturi, M.; Lavalley, J.-C. IR Study of Polycrystalline Ceria Properties in Oxidised and Reduced States. *Catal. Today* **1999**, *50*, 207–225. [CrossRef]
82. Lustemberg, P.G.; Plessow, P.N.; Wang, Y.; Yang, C.; Nefedov, A.; Studt, F.; Wöll, C.; Ganduglia-Pirovano, M.V. Vibra-tional Frequencies of Cerium-Oxide-Bound CO: A Challenge for Conventional DFT Methods. *Phys. Rev. Lett.* **2020**, *125*, 256101. [CrossRef] [PubMed]
83. Nolan, M.; Parker, S.C.; Watson, G.W. Vibrational Properties of CO on Ceria Surfaces. *Surf. Sci.* **2006**, *600*, 175–178. [CrossRef]
84. Aleksandrov, H.A.; Neyman, K.M.; Hadjiivanov, K.I.; Vayssilov, G.N. Can the State of Pla¬tinum Species Be Unambiguously Determined by the Stretching Frequency of an Adsorbed CO Probe Molecule? *Phys. Chem. Chem. Phys.* **2016**, *18*, 22108–22121. [CrossRef] [PubMed]
85. Li, C.; Sakata, Y.; Arai, T.; Domen, K.; Maruya, K.; Onishi, T. Carbon Monoxide and Carbon Dioxide Adsorption on Cerium Oxide Studied by Fourier-Transform Infrared Spectroscopy. Part 1.-Formation of Carbonate Species on Dehydroxylated $CeO_2$, at Room Temperature. *J. Chem. Soc. Faraday Trans.* **1989**, *85*, 929. [CrossRef]
86. Chen, S.; Cao, T.; Gao, Y.; Li, D.; Xiong, F.; Huang, W. Probing Surface Structures of $CeO_2$, $TiO_2$, and $Cu_2O$ Nanocrystals with CO and $CO_2$ Chemisorption. *J. Phys. Chem. C* **2016**, *120*, 21472–21485. [CrossRef]
87. Liang, B.; Andrews, L. Reactions of Laser-Ablated Ag and Au Atoms with Carbon Monoxide: Matrix Infrared Spectra and Density Functional Calculations on $Ag(CO)_n$ (n = 2, 3), $Au(CO)_n$ (n = 1, 2) and $M(CO)_n^+$ (n = 1−4; M = Ag, Au). *J. Phys. Chem. A* **2000**, *104*, 9156–9164. [CrossRef]
88. Jacox, M.E.; Thompson, W.E. The Vibrational Spectra of Molecular Ions Isolated in Solid Neon. I. $CO_2^+$ and $CO_2^-$. *J. Chem. Phys.* **1989**, *91*, 1410–1416. [CrossRef]
89. Rasko, J.; Solymosi, F. Infrared Spectroscopic Study of the Photoinduced Activation of $CO_2$ on $TiO_2$ and $Rh/TiO_2$ Catalysts. *J. Phys. Chem.* **1994**, *98*, 7147–7152. [CrossRef]
90. Binet, C.; Badri, A.; Boutonnet-Kizling, M.; Lavalley, J.-C. FTIR Study of Carbon Monoxide Adsorption on Ceria: $CO_2^{2-}$ Carbonite Dianion Adsorbed Species. *J. Chem. Soc. Faraday Trans.* **1994**, *90*, 1023. [CrossRef]
91. Kafafi, Z.H.; Hauge, R.H.; Billups, W.E.; Margrave, J.L. Carbon Dioxide Activation by Alkali Metals. 2. Infrared Spectra of $M^+CO_2^-$ and $M_2^{2+}CO_2^{2-}$ in Argon and Nitrogen Matrixes. *Inorg. Chem.* **1984**, *23*, 177–183. [CrossRef]